

See discussions, stats, and author profiles for this publication at: <https://www.researchgate.net/publication/260394546>

Characterization of the solar light field within the ocean mesopelagic zone based on radiative transfer simulations

Article in *Deep Sea Research Part I Oceanographic Research Papers* · February 2014

DOI: 10.1016/j.dsr.2014.02.005

CITATIONS

8

READS

147

3 authors, including:



Linhai Li

University of California, San Diego

20 PUBLICATIONS 176 CITATIONS

[SEE PROFILE](#)

		Volume 87	May 2014	ISSN 0967-0637
DEEP-SEA RESEARCH				
Editor: Michael P. Bacon Woods Hole, MA, USA		PART I		
		Oceanographic Research Papers		
J.E. CARTES, E. FANELLI, K. KAPIRIS, Y.K. BAYHAN, A. LIGAS, C. LÓPEZ-PÉREZ, M. MURENU, V. PAPIOL, P. RUMOLO and G. SCARCELLA		1	Spatial variability in the trophic ecology and biology of the deep-sea shrimp <i>Aristaeomorpha foliacea</i> in the Mediterranean Sea	
L.-E. HEIMBÜRGER, C. MIGNON, R. LOSNO, J.-C. MIQUEL, B. THIBODEAU, M. STABHOLZ, A. DUFOR and N. LEBLOND		14	Vertical export flux of metals in the Mediterranean Sea	
P. MATEU, F.E. MONTERO and M. CARRASSÓN		24	Geographical variation in metazoan parasites of the deep-sea fish <i>Bathyporeia mediterranea</i> Bauchot, 1962 (<i>Osteichthyes: Ipnopidae</i>) from the Western Mediterranean	
Z. ZHANG, F. QIAO and J. GUO		30	Subsurface eddies in the southern South China Sea detected from in-situ observation in October 2011	
P.G. BREWER, A.F. HOFMANN, E.T. PELTZER and W. USSLER, III		35	Evaluating microbial chemical choices: The ocean chemistry basis for the competition between use of O ₂ or NO ₃ as an electron acceptor	
Q. YANG, J. TIAN, W. ZHAO, X. LIANG and L. ZHOU		43	Observations of turbulence on the shelf and slope of northern South China Sea	
L. LI, D. STRAMSKI and R.A. REYNOLDS		53	Characterization of the solar light field within the ocean mesopelagic zone based on radiative transfer simulations	
D. CUVELIER, J. BEESAU, V.N. IVANENKO, D. ZEPPIILLI, P.-M. SARRADIN and J. SARRAZIN		70	First insights into macro- and meiofaunal colonisation patterns on paired wood/slate substrata at Atlantic deep-sea hydrothermal vents	
M.R. WADLEY, T.D. JICKELLS and K.J. HEYWOOD		82	The role of iron sources and transport for Southern Ocean productivity	
		www.elsevier.com/locate/dsri		

This article appeared in a journal published by Elsevier. The attached copy is furnished to the author for internal non-commercial research and education use, including for instruction at the authors institution and sharing with colleagues.

Other uses, including reproduction and distribution, or selling or licensing copies, or posting to personal, institutional or third party websites are prohibited.

In most cases authors are permitted to post their version of the article (e.g. in Word or Tex form) to their personal website or institutional repository. Authors requiring further information regarding Elsevier's archiving and manuscript policies are encouraged to visit:

<http://www.elsevier.com/authorsrights>



Contents lists available at ScienceDirect

Deep-Sea Research I

journal homepage: www.elsevier.com/locate/dsrI

Characterization of the solar light field within the ocean mesopelagic zone based on radiative transfer simulations



Linhai Li^{*}, Dariusz Stramski, Rick A. Reynolds

Marine Physical Laboratory, Scripps Institution of Oceanography, University of California San Diego, La Jolla, CA 92093-0238, USA

ARTICLE INFO

Article history:

Received 9 October 2013
Received in revised form
3 February 2014
Accepted 4 February 2014
Available online 25 February 2014

Keywords:

Ocean optics
Underwater light field
Asymptotic light field
Apparent optical properties
Mesopelagic zone
Radiative transfer modeling

ABSTRACT

The solar light field within the ocean from the sea surface to the bottom of the mesopelagic zone was simulated with a radiative transfer model that accounts for the presence of inelastic radiative processes associated with Raman scattering by water molecules, fluorescence of colored dissolved organic matter (CDOM), and fluorescence of chlorophyll-*a* contained in phytoplankton. The simulation results provide a comprehensive characterization of the ambient light field and apparent optical properties (AOPs) across the entire visible spectral range within the depth range 200–1000 m of the entire mesopelagic zone for varying chlorophyll-*a* concentration and seawater optical properties in the mixed surface layer of the ocean. With increasing depth in the mesopelagic zone, the solar irradiance is reduced by ~9–10 orders of magnitude and exhibits a major spectral maximum in the blue, typically centered around a light wavelength of 475 nm. In the green and red spectral regions, the light levels are significantly lower but still important owing to local generation of photons via inelastic processes, mostly Raman scattering and to a lesser extent CDOM fluorescence. The Raman scattering produces a distinct secondary maximum in irradiance spectra centered around 565 nm. Comparisons of our results with light produced by the radioactive decay of the unstable potassium isotope contained in sea salt (⁴⁰K) indicates that the solar irradiance dominates over the ⁴⁰K-produced irradiance within the majority of the mesopelagic zone for most scenarios considered in our simulations. The angular distribution of radiance indicates the dominance of downward propagation of light in the blue and approach to uniform distribution in the red throughout the mesopelagic zone. Below the approximate depth range 400–500 m, the shape of the angular distribution is nearly invariant with increasing depth in the green and red and varies weakly in the blue. The AOPs at any light wavelength also assume nearly constant values within the deeper portion of the mesopelagic zone. These results indicate that the mesopelagic light field reaches a nearly-asymptotic regime at depths exceeding ~400–500 m.

© 2014 Elsevier Ltd. All rights reserved.

1. Introduction

The mesopelagic zone of the deep ocean is the middle layer of the water column extending between depths of 200 m and 1000 m. This layer is bordered above by the well-illuminated epipelagic (photic) zone in which there is sufficient amount of solar light to support the process of photosynthesis, and below by the aphotic bathypelagic zone in which there is virtually no solar light or the light level is extremely low (at least a few orders of magnitude below 10^{-10} of full sunlight). As a small amount of light penetrates the mesopelagic zone, this layer is also referred to as the twilight zone. This zone provides a large worldwide habitat for a diverse community of deep-sea animals with unique adaptations, which

include the ability to gather low levels of ambient light with large eyes (Denton, 1990; Warrant, 2004; Warrant and Locket, 2004), produce light from bioluminescent organs (Boden and Kampa, 1974; Haddock et al., 2010; Widder, 2010), or undergo diel vertical migrations to the surface layer to feed at night (Hays, 2003; Cohen and Forward, 2009). The adaptations, behavioral patterns, and activities of deep-sea animals can be affected by the ambient light field that undergoes large vertical changes within the water column (Denton, 1990; Widder and Frank, 2001, 2004; Johnsen, 2005). Many deep-sea animals exhibit various responses to changing optical conditions, which are commonly associated with camouflage strategies, counter adaptations for breaking camouflage, or vertical migrations (Denton, 1970; Denton et al., 1972; Herring and Roe, 1988; McFall-Ngai, 1990; Widder and Frank, 2001; Johnsen, 2005; Zylinski and Johnsen, 2011). For example, mesopelagic organisms have developed specific adaptations of visual systems to increase sensitivity to the dim ambient light, and some

^{*} Corresponding author. Tel.: +1 858 822 4908.

E-mail address: lii032@ucsd.edu (L. Li).

organisms can likely detect ambient light at depths as large as 1000 m (Clarke and Denton, 1962; Denton, 1990; Warrant and Locket, 2004).

Although the importance of the optical environment for deep-sea organisms has long been recognized, the vertical variations in the magnitude, spectral composition across the entire visible spectrum, and angular distribution of ambient solar light throughout the entire mesopelagic zone have not been thoroughly investigated and documented. The commonly known basic features of variation in the underwater light field with increasing depth are that light intensity decreases approximately exponentially, the spectrum of light narrows becoming increasingly blue, and the angular distribution of light becomes more symmetrical around the vertical axis (Jerlov, 1976). Typically, the general characterization of the ambient light at mesopelagic depths entails dim, nearly monochromatic, and primarily downwelling solar radiation (Kampa, 1970; Jerlov, 1976; Denton, 1990; Johnsen et al., 2004; Warrant and Locket, 2004). Such a characterization of the mesopelagic light field has been based primarily on studies whose main focus was on the blue spectral region owing to interest in various adaptations and activities of deep-sea animals, such as blue sensitivity of visual systems (Frank and Case, 1988; Frank and Widder, 1999; Warrant and Locket, 2004) and bioluminescence, the vast majority of which lies in the blue and blue-green spectral region with a maximal emission between light wavelengths of 440 and 510 nm (Herring, 1983; Latz et al., 1988; Haddock and Case, 1999).

Studies involving direct measurements of ambient solar light at mesopelagic depths have been rare. The first deep-sea radiometric measurements of ambient daylight were conducted in a series of experiments in Atlantic waters down to depths of about 600–700 m using an irradiance meter capable of measuring light intensities as low as 10^{-12} of full sunlight (Clarke and Wertheim, 1956; Clarke and Kelly, 1965). These data have, however, significant limitations for characterizing the light field because of very broad spectral sensitivity of the instrument, covering the range of light wavelengths from approximately 320 nm to 650 nm with a maximum at 480 nm. Irradiance measurements within a broad spectral range (Full Width Half-Maximum, FWHM, of ~ 50 nm) centered at 515–520 nm down to a depth of 400 m were also made by investigators from the former Soviet Union (Ochakovskii et al., 1974). The first spectral radiometric measurements within the mesopelagic zone were performed with a highly-sensitive irradiance meter equipped with several interference filters having a narrow bandwidth (FWHM of ~ 10 nm) and covering a spectral range from about 410 nm to 540 nm (Boden et al., 1960; Kampa, 1970). Despite the fact that the study of Kampa (1970) was conducted over 40 years ago, to our knowledge it still provides the most comprehensive set of radiometric measurements within the mesopelagic zone to date. These measurements were made in four regions of the eastern North Atlantic and provided data of spectral downward irradiance between 408 and 533 nm at mesopelagic depths as large as 615 m. In more recent years, field experiments with deep-sea light measurements are very scarce and were limited to measuring the downward irradiance at a single narrow waveband centered at 480 nm (FWHM of 10 nm) or within a broader waveband simulating the spectral sensitivity of the eyes of a vertically migrating shrimp (Widder and Frank, 2001; Frank and Widder, 2002; Myslinski et al., 2005).

Because the amount and scope of information available from deep-sea light measurements is limited, theoretical studies of radiative transfer in the ocean offer a particularly important approach for advancing the knowledge and understanding of various characteristics of the mesopelagic light field. However, despite numerous efforts devoted to radiative transfer within the surface photic layer, only a few studies included simulations of the

light field at mesopelagic depths and the reported results were significantly limited in scope (Berwald et al., 1998; Johnsen et al., 2004; Johnsen, 2005). Among these previous studies the most comprehensive suite of simulations was presented in Berwald et al. (1998). However, these simulations did not extend to large mesopelagic depths below 600 m and the reported results were limited mostly to vertical profiles and spectra of two apparent optical properties (AOPs) derived from simulated plane and scalar irradiances, namely the diffuse attenuation coefficient for net irradiance, K_E , and the average cosine of the light field, $\bar{\mu}$ (see Mobley (1994) for details on terminology and definitions in hydrologic optics). No information on radiometric quantities was explicitly reported. Also, whereas the simulations included Raman scattering by water molecules, other inelastic radiative processes (i.e., transpectral processes in which the wavelength changes during an interaction of radiation with the medium) such as fluorescence of colored dissolved organic matter (CDOM) and chlorophyll-*a* were not included, reducing the realism of the simulated light fields. The studies of Johnsen et al. (2004) and Johnsen (2005) focused on cryptic strategies of deep-sea animals and reported very limited data from radiative transfer simulations, specifically the spectral shapes of downwelling irradiance at two mesopelagic depths (200 and 800 m) and reflectance for the lateral surface at depths extending to 450 m as derived from horizontal radiances and irradiances. Limited data of irradiance for the uppermost portion of mesopelagic zone (200 and 300 m) are also presented in Johnsen (2012). In all these previous theoretical studies Raman scattering was included in the simulations but fluorescence processes were not.

This brief overview of previous experimental and theoretical studies indicates that current knowledge of the mesopelagic light field is critically limited with regard to several aspects of light field characterization, including vertical variations in the magnitude and spectral composition of various radiometric quantities (radiance and various types of irradiance) across the entire visible spectral range as well as the angular distribution of spectral radiance throughout the entire mesopelagic zone. One specific area that requires further investigation concerns the light field in the green and red spectral regions, in which inelastic radiative processes, especially Raman scattering, play a dominant role at mesopelagic depths (Berwald et al., 1998). Another specific area of interest concerns the approach of the actual light field to the so-called asymptotic regime. With increasing depth in the ocean, the light field undergoes transformation and can achieve a nearly-asymptotic or possibly an asymptotic state at sufficiently large depths. In this state, which depends only on the inherent optical properties (IOPs) of seawater, the shape of the angular distribution of radiance is constant, and the radiance in every direction and irradiances all decrease with depth at the same exponential rate. This rate is constant with depth if IOPs do not change. In addition, the asymptotic radiance distribution is rotationally symmetric around the vertical and independent of illumination conditions at the sea surface. The existence of the asymptotic light field with such properties was proven theoretically many years ago for a hypothetical homogeneous ocean without inelastic processes and internal sources of light (Preisendorfer, 1959; Højerslev and Zaneveld, 1977). Although such predictions were unrealistic due to the absence of inelastic processes that play an increasingly important role with increasing depth, the critical significance of these processes for the approach of light field towards the asymptotic regime was recognized only in the 1990s (Gordon et al., 1993; Gordon and Xu, 1996; Berwald et al., 1998).

In particular, the radiative transfer simulations of Berwald et al. (1998) demonstrated that in the presence of Raman scattering (no fluorescence included) the two AOPs, K_E , and $\bar{\mu}$, reach nearly-asymptotic values at mesopelagic depths. In the green and red

spectral regions, these values were shown to differ dramatically from their counterparts obtained under the assumption of no Raman scattering. Berwald et al. (1998) did not, however, examine the shape of the angular distribution of radiance, a main diagnostic property of the asymptotic field. A more comprehensive analysis of light field characteristics throughout the entire mesopelagic zone is therefore required to establish better understanding of the nearly-asymptotic light field or potential existence of truly asymptotic regime in the deep ocean under realistic conditions when both Raman scattering and fluorescence are present. Such understanding can have practical implications for potential determinations of the deep-sea light field from radiometric measurements. Measurements taken throughout the water column down to the top of the nearly-asymptotic or asymptotic layer only would be sufficient to predict the light field at larger depths if the IOPs of seawater remain constant or nearly constant with depth. It is expected that this IOP scenario is often a reasonable approximation at large mesopelagic depths.

In this study, the solar light field within the water column from the sea surface throughout the epipelagic and entire mesopelagic zone of the ocean was simulated with a radiative transfer model that included the inelastic processes of Raman scattering by water molecules and fluorescence of CDOM and chlorophyll-*a*. On the basis of these simulations, our primary objective is to present a comprehensive characterization of the mesopelagic light field, including the magnitudes and spectral composition of radiance and irradiance, the angular distribution of spectral radiance, and major AOPs, namely irradiance reflectance, average cosines and diffuse attenuation coefficients, for a broad range of IOPs within the ocean surface layer. Our intent is to also provide an improved understanding of the roles of Raman scattering and CDOM fluorescence for the mesopelagic light and the formation of nearly-asymptotic light field at mesopelagic depths. In addition to persistent light levels associated with solar photons that reach mesopelagic depths during daylight hours, there also exists a background of light produced by the radioactive decay of an unstable potassium isotope (^{40}K) contained in sea salt. Our results provide a basis for rigorous comparison of solar and ^{40}K -produced light levels within the ocean mesopelagic zone.

2. Radiative transfer simulations

The light field between the sea surface and a depth of 1000 m was simulated using the scalar radiative transfer model Hydro-light 5.1.4 from Sequoia Scientific, Inc. (Mobley, 1994; Mobley and Sundman, 2008). This model computes the full angular distribution of spectral radiance $L(z, \theta, \phi, \lambda)$ at each preselected output depth z in the ocean (positive downward), where θ is the zenith (or nadir) angle and ϕ is the azimuth angle which together identify the direction of light propagation, and λ the wavelength of light in vacuum. The zenith (θ_z) and nadir (θ_n) angles represent the direction of photon travel relative to the vertical. In the case of downwelling radiance, L_d , this direction is defined by the nadir angle θ_n , and for the upwelling radiance, L_u , the zenith angle θ_z . For the special case of

$\theta_n=0$, the radiance L_d is associated with photons that travel along the vertical straight in the downward direction. Similarly, for $\theta_z=0$, the radiance L_u is associated with photons that travel along the vertical straight in the upward direction. Note that the angles θ_n and θ_z range from -90° to $+90^\circ$, where the sign depends on the portion of the azimuthal plane within which the radiance is calculated. For example, for the solar principal plane the positive values of θ_n and θ_z are within the half-plane containing the sun, and the negative values within the opposite half-plane. The azimuth angle $\phi=0^\circ$ corresponds to the half-plane of the solar principal plane containing the sun, and $\phi=180^\circ$ to the opposite half-plane. The azimuth angle varies clockwise between 0° and 360° .

The simulations were conducted at 5 nm intervals within the spectral range from 350 to 700 nm, and over the depth range from the sea surface to 1000 m. Outputs of the simulations were saved at 10 m depth intervals. The various irradiances and apparent optical properties (AOPs) were calculated from the radiance distribution.

2.1. Simulation design and boundary conditions

Vertical profiles of the inherent optical properties (IOPs) of seawater, including the total spectral absorption coefficient $a(\lambda)$, spectral scattering coefficient $b(\lambda)$, and spectral scattering phase function $\tilde{p}(\psi, \lambda)$ associated with elastic scattering by water molecules and suspended particles (where ψ is the scattering angle), are required inputs for each simulation. In this study, we assume a “three-layer ocean” by specifying different IOPs for three depth layers. The surface mixed layer (ML) is the uppermost illuminated layer of the ocean, which is characterized by the presence of phytoplankton and other optically significant constituents that are typically associated with or derived from phytoplankton productivity, such as CDOM and detrital particles. The transition layer (TL) in our simulations is defined as an intermediate layer within the water column located between the base of the ML and the top of the deep layer (DL). The DL extends to the base of the mesopelagic zone at 1000 m depth and further beyond that depth as we assume an infinitely deep ocean in our simulations. The DL contains no phytoplankton but does contain small amounts of non-phytoplankton particles and CDOM that originate from the downwelling transport from surface layers (e.g., convective mixing, meridional overturning circulation) and local biological activities and interactions in the deep layer.

We examined three basic scenarios of the three-layer model, each with a different value of chlorophyll-*a* concentration (*Chl*) within the ML and different layer thicknesses (Table 1). To represent a scenario of ultra-oligotrophic conditions characterized by very clear surface waters, a *Chl* value of 0.02 mg m^{-3} was used within a ML extending from the surface to a depth of 200 m. In this case the TL extends from 200 m to 270 m, and the DL from 270 m to infinity. For the intermediate case of *Chl* = 0.2 mg m^{-3} , the depth range for the ML is 0–100 m, for the TL 100–150 m, and the DL extends below 150 m. Finally, for simulations in which *Chl* = 2 mg m^{-3} the ML extends down to only 30 m, the TL from 30

Table 1

Description of simulation scenarios. Depth intervals of the mixed and transition layers for each scenario of mixed layer chlorophyll-*a* concentration, *Chl*, were based on the study of Uitz et al. (2006), and the deep layer was assumed to be infinitely deep. All 18 simulations were conducted with a solar zenith angle of 30° and a wind speed of 5 m s^{-1} , with output saved at 10 m depth intervals. Simulations were done over the spectral range 350 to 750 nm at 5 nm increments.

<i>Chl</i> in ML (mg m^{-3})	0.02	0.2	2
Layer depths (m)			
Mixed layer, ML	0–200	0–100	0–30
Transition layer, TL	200–270	100–150	30–60
Deep layer, DL	270–∞	150–∞	60–∞
Cloud cover	Clear sky or 100% overcast sky		
Inelastic processes	(i) None, (ii) Raman scattering only, (iii) Raman scattering, CDOM and chlorophyll- <i>a</i> fluorescence		

to 60 m, and the DL below 60 m. We note that $Chl=0.2 \text{ mg m}^{-3}$ is similar to the global mean values of surface Chl of $\sim 0.22\text{--}0.26 \text{ mg m}^{-3}$ estimated from satellite observations (Gregg and Conkright, 2002), and this case is shown in this paper preferentially when reporting results from a single Chl scenario.

The selection of thicknesses for the ML and TL was based on the analysis of vertical profiles of Chl in vertically-mixed oceanic waters as described in the study of Uitz et al. (2006), and represent situations in which the depth of the euphotic zone is located within the surface mixed layer. We assumed that the IOPs within the ML and DL are independent of depth, but differ from each other and among the three Chl scenarios. In contrast, the IOPs within the TL vary with depth and are calculated from spline interpolation between the values of the ML and DL. We recall that the chlorophyll- a concentration is always zero within the DL. This implies no chlorophyll- a within the entire mesopelagic zone in all our simulations with one exception of very small levels of Chl ($< 0.02 \text{ mg m}^{-3}$) within the TL between 200 and 270 m for the ultra-oligotrophic case in which Chl in the ML was assumed to equal 0.02 mg m^{-3} .

Boundary conditions and other ancillary information for the simulations are also summarized in Table 1. Specifically, for each Chl scenario we performed the simulations with a solar zenith angle of 30° , two different sky conditions (clear and overcast), and a wind speed of 5 m s^{-1} to determine sea surface roughness. An infinitely-deep ocean was assumed in all simulations.

2.2. Determinations of inherent optical properties of seawater

The input IOPs of seawater were specified within the spectral range from 350 to 700 nm at 1 m depth intervals. For simplicity the symbol of depth, z , is omitted in the notation of IOPs below. The spectral absorption coefficient, $a(\lambda)$, within the ML was modeled as a sum of three component coefficients representing the molecular absorption of pure water, $a_w(\lambda)$, suspended particles, $a_p(\lambda)$, and CDOM, $a_g(\lambda)$:

$$a(\lambda) = a_w(\lambda) + a_p(\lambda) + a_g(\lambda), \quad (1)$$

Values of $a_w(\lambda)$ within the spectral ranges of 350–380 nm and 380–750 nm were obtained from the measurements of Sogandares and Fry (1997) and Pope and Fry (1997), respectively. The coefficients $a_p(\lambda)$ and $a_g(\lambda)$ were calculated from Chl using the “New Case 1” bio-optical model embedded within Hydrolight (Mobley and Sundman, 2008). In brief, particulate absorption was modeled as a power function of chlorophyll- a concentration

$$a_p(\lambda) = A(\lambda)Chl^{B(\lambda)}, \quad (2)$$

where $A(\lambda)$ and $B(\lambda)$ are wavelength dependent parameters determined from field studies (Bricaud et al., 1998; Vasilkov et al., 2005). The value of $a_g(\lambda)$ was also assumed to vary with Chl and calculated from the relation

$$a_g(\lambda) = a_g(440)e^{-S \times (\lambda - 440)} = 0.2a_p(440)e^{-S \times (\lambda - 440)}, \quad (3)$$

where the spectral slope parameter S was set to 0.018 nm^{-1} . This value was chosen as representative of surface waters from the study of Nelson et al. (2010).

The spectral scattering coefficient, $b(\lambda)$, within the ML was calculated as the sum of scattering by pure seawater, $b_w(\lambda)$, and suspended particles, $b_p(\lambda)$,

$$b(\lambda) = b_w(\lambda) + b_p(\lambda), \quad (4)$$

Values of $b_w(\lambda)$ were obtained from Morel (1974) (see also Mobley, 1994) and $b_p(\lambda)$ was calculated according to Morel et al. (2002)

$$b_p(\lambda) = 0.416Chl^{0.766} \left(\frac{\lambda}{550} \right)^v, \quad (5a)$$

where the exponent v was parameterized as

$$v = \begin{cases} 0.5(\log_{10} Chl - 0.3), & 0.02 \leq Chl \leq 2 \\ 0, & Chl > 2 \end{cases}, \quad (5b)$$

Within the DL, the absorption coefficient $a(\lambda)$ was assumed to have no particulate contribution as particles generally account for less than 10% of absorption at depths corresponding to the DL in our simulations (Nelson et al., 2010). Values of $a_g(\lambda)$ in the DL were assumed constant and computed from Eq. (3) with $a_g(440) = 0.018 \text{ m}^{-1}$ and $S = 0.018 \text{ nm}^{-1}$. These values correspond to approximate average values for mesopelagic depths below 200 m reported in the study of Nelson et al. (2010). The calculation of the spectral scattering coefficient within this layer was adopted from Berwald et al. (1998),

$$b(\lambda) = b_w(\lambda) + b_p(550) \left(\frac{550}{\lambda} \right), \quad (6)$$

where the magnitude of $b_p(550)$ is assumed to be 0.005 m^{-1} and the spectral shape of $b_p(\lambda)$ varies as λ^{-1} . Importantly, the IOPs within the DL are the same for all simulations regardless of assumed surface conditions, and thus the three Chl scenarios differ only with regards to IOPs within the ML and TL. Fig. 1 depicts the vertical profiles of the beam attenuation coefficient, $c(\lambda) = a(\lambda) + b(\lambda)$, at two example light wavelengths (480 and 660 nm), which were used in our simulations.

The final IOP required as input to the RT simulations is the spectral scattering phase function characterizing the angular shape of the spectral volume scattering function (Mobley, 1994). The phase function of pure seawater, $\beta_w(\psi, \lambda)$, and an average phase function of suspended particles, $\beta_p(\psi, \lambda)$, determined from measurements of Petzold (1972) were used for all simulations and assumed to be depth-invariant.

The IOP profiles generated for the idealized three-layer ocean do not exactly reproduce specific environmental conditions and are not intended to necessarily represent all features observable in the ocean, such as potential vertical variations in IOPs caused by deep chlorophyll maxima, particle concentration maxima, or different water masses (Jerlov, 1976; Kitchen and Zaneveld, 1990). The current knowledge about vertical profiles of IOPs is fragmentary because typical field experiments do not include simultaneous

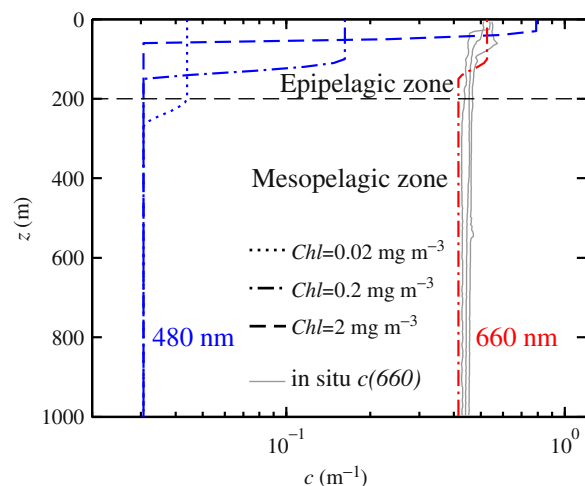


Fig. 1. Vertical profiles of the modeled beam attenuation coefficient, $c(\lambda)$, at 480 nm and 660 nm for the three simulation scenarios of varying chlorophyll- a concentration (Chl) in the mixed layer as indicated for different line types. The profile of $c(660)$ is depicted for the intermediate chlorophyll- a concentration only, but for comparison three in situ measurements of $c(660)$ obtained during the 2005 ANT-XXIII cruise in the eastern Atlantic Ocean are also illustrated.

measurements of all IOPs and the measured IOPs are often limited in terms of spectral information, depth range, or depth resolution. Such fragmentary data are particularly scarce in the mesopelagic zone. Therefore, a modeling study of an idealized three-layer ocean represents an approach that is both practically feasible and reasonable. We also note that the degree of realism in our assumptions of homogeneous ML and DL layers, higher values of IOPs in the ML than DL, and gradually decreasing IOPs with depth in the TL appears sufficient for the main purposes of our study. Example deep-sea measurements supporting our assumptions are depicted in Fig. 1. Example measurements of the beam attenuation coefficient at 660 nm, $c(660)$, acquired during the ANT-XXIII cruise in the Atlantic Ocean (Stramski et al., 2008) show a similar magnitude (0.425 m^{-1}) to our simulated values in the DL (0.415 m^{-1}) and little vertical structure within the mesopelagic zone. Additionally, values for the CDOM absorption coefficient for the DL assumed in this study (e.g., 0.091 m^{-1} at 350 nm) are within the range of deep-sea measurements of CDOM absorption ($0.065\text{--}0.10 \text{ m}^{-1}$ at 350 nm) made during the same cruise (Röttgers and Doerffer, 2007).

2.3. Inelastic radiative processes

Inelastic radiative processes represented in the model simulations included Raman scattering by water molecules, fluorescence by CDOM, and fluorescence by chlorophyll-*a*. These processes generally involve excitation by shorter wavelength photons and emission of longer wavelength photons. A detailed description of the use of inelastic processes in radiative transfer models including the Hydrolight model is provided in Mobley et al. (1993) and Mobley (1994). We used the default options of Hydrolight 5.1.4 for the Raman scattering coefficient at a reference wavelength of 488 nm and the wavelength dependence of this coefficient, which are based on studies of Bartlett et al. (1998) and Desiderio (2000). For the sake of computational simplicity, the Hydrolight model assumes an isotropic Raman scattering phase function $\tilde{\beta}_{\text{Raman}}(\psi) = 1/4\pi$ (C. Mobley, personal communication) instead of the commonly accepted function of $\tilde{\beta}_{\text{Raman}}(\psi) = 0.067 \times (1 + 0.55 \cos^2 \psi)$ (Mobley, 1994). This simplification will have some effect on the computed radiance field $L(z, \theta, \phi, \lambda)$, in particular at mesopelagic depths within the green and red spectral regions, but yields the correct contribution of Raman scattering to irradiances, which are computed from azimuthally averaged radiance, as well as the apparent optical properties which are computed from irradiances. Therefore, this simplified formalism is not expected to invalidate the general patterns of the results and main conclusions of this study. In addition, we expect that small uncertainties within $< 10\%$ in the parameters quantifying Raman scattering (Bray et al., 2013) have no significant effect on the key results of our study because Raman scattering produces very large quantitative and qualitative changes in the mesopelagic light field as discussed below. The Hydrolight model also assumes an isotropic fluorescence emission by CDOM and chlorophyll-*a*, which is justified as the angular distribution of light produced by fluorescence is typically isotropic or nearly isotropic (e.g., Gordon et al., 1993). Because the spectral quantum efficiency functions of CDOM fluorescence and chlorophyll-*a* fluorescence vary to some extent for various water bodies, the Hydrolight model utilizes the functions that represent typical or approximately average levels of fluorescence observed in the ocean. Specifically, for modeling CDOM fluorescence, Hydrolight uses the spectral fluorescence quantum efficiency that is a function of both the excitation and emission wavelengths as depicted in Fig. 5.11 in Mobley (1994). This function is based on measurements of natural water samples (Hawes, 1992; Hawes et al., 1992). For chlorophyll-*a* fluorescence Hydrolight uses the quantum efficiency of 0.02 independent of excitation wavelength, which is within a range of typical values between 0.01 and

0.05 (Mobley, 1994). This formalism for modeling the fluorescence processes is satisfactory for the purposes of our simulations, especially because we do not aim at simulating some specific location in the ocean at some specific time.

For each simulation scenario representing specific sky conditions and *Chl* in the ML, three different Hydrolight runs were performed with different cases of inelastic processes; (i) no inelastic processes, (ii) Raman scattering only, and (iii) Raman scattering and fluorescence of both CDOM and chlorophyll-*a*. The three scenarios of surface *Chl*, two scenarios of sky conditions, and three scenarios of inelastic processes described in Table 1 result in a total of 18 discrete simulations. On the basis of these simulations we describe the vertical light field in terms of fundamental radiometric quantities such as radiance and different irradiances, and additionally report selected AOPs such as irradiance reflectance, average cosines of the light field, and the diffuse attenuation coefficients. All reported radiometric quantities and AOPs generally depend on both z and λ , but for the sake of brevity this dependence is not specified in notation except in cases of ambiguity. We restrict interpretation of simulation results to the visible spectral range 400–700 nm. Note that the simulations included the range 350–400 nm to properly account for the contributions of inelastic processes to the visible spectral range. Because of our interest in the mesopelagic zone, the discussion of results is focused on depths between 200 and 1000 m.

3. Results and discussion

3.1. Irradiance field

The scalar irradiance, E_o , quantifies the total amount of radiant energy incident on a surface per unit area and per unit time at any given depth in the ocean. Fig. 2 depicts vertical profiles of E_o at selected light wavelengths (440, 550, and 660 nm) and the spectra of E_o at selected depths (1, 200, 500, 800, and 1000 m). These results were obtained from simulations for clear skies and the three scenarios of chlorophyll-*a* concentration, *Chl*, within the surface mixed layer. In addition, each panel in Fig. 2 illustrates results for the three scenarios involving the presence or absence of inelastic processes. The first case without inelastic processes, although unrealistic, can be considered a baseline result in which only absorption and elastic scattering determine the light field. The second case includes Raman scattering but no fluorescence processes. The third case includes Raman scattering and fluorescence processes associated with both CDOM and chlorophyll-*a*, and is the most representative of natural oceanic waters.

The spectral range of 400–500 nm exhibits maximal values of E_o (Fig. 2). In this range the curves corresponding to the cases with and without inelastic processes are nearly indistinguishable, suggesting that the effects of these processes on E_o are very small or negligible. Values of E_o at the top of mesopelagic zone (i.e., 200 m) are reduced compared with the surface values by approximately 2 orders of magnitude in very clear waters when $Chl=0.02 \text{ mg m}^{-3}$, 4 orders of magnitude when $Chl=0.2 \text{ mg m}^{-3}$, and 5–6 orders of magnitude when $Chl=2 \text{ mg m}^{-3}$. For the simulation representing clear skies and minimal surface *Chl*, the maximum value of E_o at 200 m occurs at a wavelength of 415 nm with a magnitude of about $6.7 \times 10^{-2} \text{ W m}^{-2} \text{ nm}^{-1}$. At the bottom of the mesopelagic zone at $z=1000 \text{ m}$, the maximum spectral E_o is reduced to $1.2 \times 10^{-11} \text{ W m}^{-2} \text{ nm}^{-1}$ and shifted to a wavelength of 475 nm. For the scenarios with higher *Chl*, the values of E_o within the mesopelagic zone are naturally much lower. For $Chl=0.2 \text{ mg m}^{-3}$, the maximum spectral E_o is $7.1 \times 10^{-4} \text{ W m}^{-2} \text{ nm}^{-1}$ at $z=200 \text{ m}$ and $3.2 \times 10^{-13} \text{ W m}^{-2} \text{ nm}^{-1}$ at 1000 m. These maxima both occur at $\lambda=475 \text{ nm}$ which is the most penetrating light wavelength throughout

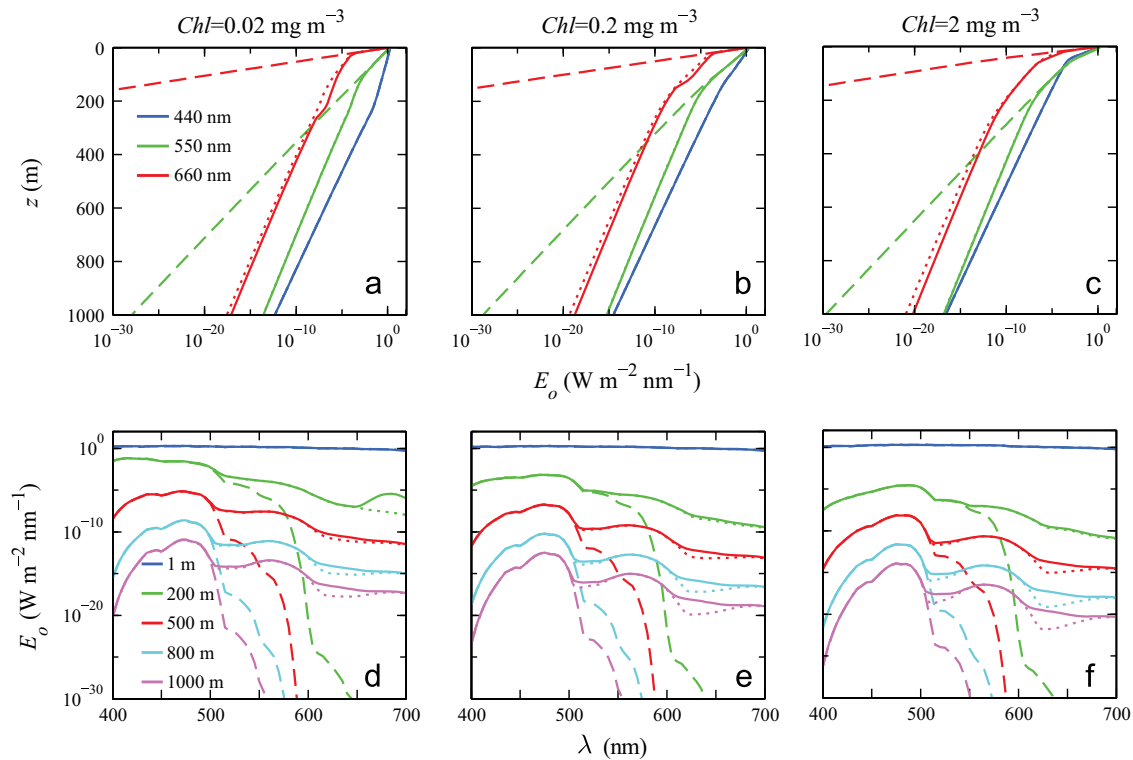


Fig. 2. (a–c) Vertical profiles of the scalar irradiance, $E_o(\lambda)$, at selected light wavelengths as indicated for the three simulation scenarios of varying Chl with clear sky conditions. (d–f) Spectra of $E_o(\lambda)$ at selected depths as indicated for the same simulation scenarios. In each panel, dashed lines represent the simulations with no inelastic processes, dotted lines the cases with Raman scattering included, and solid lines the cases which include Raman scattering and the fluorescence of CDOM and chlorophyll-*a*.

the entire mesopelagic zone for this Chl case. For the most turbid surface layer considered in our study with $Chl=2 \text{ mg m}^{-3}$, the maximum spectral E_o at 200 m is $2.8 \times 10^{-5} \text{ W m}^{-2} \text{ nm}^{-1}$ at $\lambda=490 \text{ nm}$. At 1000 m, the maximum is $1.2 \times 10^{-14} \text{ W m}^{-2} \text{ nm}^{-1}$ at 475 nm. For the simulations representing overcast sky conditions, the magnitude of E_o within the mesopelagic zone regardless of the depth is typically reduced 4–5-fold compared with clear sky conditions (not shown). We also recall that our simulations were made for a single solar zenith angle of 30° . The underwater irradiance would generally decrease in response to increasing solar zenith angle.

These results demonstrate a very large dynamic range of irradiance within the mesopelagic zone. In the blue spectral range where the irradiance exhibits maximum values, E_o decreases by about 9–10 orders of magnitude between the top and bottom of the mesopelagic zone. In addition, an increase in the surface Chl by 2 orders of magnitude results in a reduction of E_o at mesopelagic depths by about 3 orders of magnitude. The spectral location of the E_o maximum at the top of mesopelagic zone depends on the surface Chl , shifting from 415 nm to 490 nm as Chl increases from 0.02 to 2 mg m^{-3} . However, at depths below about 800 m the E_o maximum is located consistently around 475 nm regardless of surface Chl . Johnsen et al. (2004) also reported that the wavelength of maximum light penetration can shift slightly from 490 nm at 200 m to 480 nm at 800 m, which is consistent with our results for $Chl=2 \text{ mg m}^{-3}$. The wavelength corresponding to peak transmission and its possible spectral shifts may have implications to bioluminescent emission and vision sensitivity of mesopelagic animals, as it is likely that many organisms can adjust bioluminescent, cryptic, or visual abilities in response to changes in the mesopelagic optical environment (Warrant and Lockett, 2004; Johnsen, 2012). Our simulations suggest that the magnitude and spectral composition of the light field within this environment

is strongly affected by the optical properties within the overlying epipelagic layer.

The influence of inelastic radiative processes on the mesopelagic light field is much more pronounced at wavelengths exceeding 500 nm than in the blue (Fig. 2). In the absence of inelastic processes, the magnitude of E_o at mesopelagic depths decreases sharply with increasing wavelength for $\lambda > 500 \text{ nm}$. Our simulations suggest that without consideration of inelastic processes, the computed magnitudes of E_o at 1000 m depth approach values as low as $10^{-100} \text{ W m}^{-2} \text{ nm}^{-1}$. When inelastic processes are included, however, E_o at 1000 m remains greater than $10^{-21} \text{ W m}^{-2} \text{ nm}^{-1}$ within the green and red parts of the visible spectral range. These results suggest that if we consider light within the mesopelagic zone which ultimately originates from solar radiation, then the observable photons at $\lambda > 500 \text{ nm}$ are almost entirely generated by inelastic processes of Raman scattering and CDOM fluorescence in water.

Further inspection of the results depicted in Fig. 2 indicates that Raman scattering is the primary inelastic process contributing to the mesopelagic light field within this spectral range (i.e., $\lambda > 500 \text{ nm}$). The fluorescence by CDOM plays a significant role within two distinct spectral regions, namely the region 505–530 nm with a maximum effect at 510 nm and the region 610–670 nm with a maximum effect at 620 nm. The spectra of E_o exhibit distinct minima within these spectral regions for the simulations including Raman scattering but excluding CDOM fluorescence. When both Raman scattering and CDOM fluorescence were included in the simulations, these minima are much less pronounced, indicating a significant additional contribution of CDOM fluorescence to E_o at these wavelengths. This pattern is associated with the interplay of the processes of Raman scattering and CDOM fluorescence, including the effects caused by the differences in the spectral redistribution functions for these

Table 2

Relative contributions of three sources to the submarine light field which ultimately originate from solar radiation; first, solar photons that have not undergone any transpectral process, i.e., elastically scattered solar photons plus direct solar photons denoted as Solar(e+d), second, Raman-scattered photons denoted as Raman, and third, CDOM and chlorophyll-*a* fluorescence photons denoted as Fluorescence. At mesopelagic depths the component of Solar(e+d) associated with direct solar photons is expected to be very small. Results are from the simulation with $Chl=0.2 \text{ mg m}^{-3}$ in the surface mixed layer and clear sky conditions. Contributions from each source are listed in percent. The summed values do not exactly equal 100% because of rounding.

Depth (m)		1	200	500	800	1000
λ (nm)	Source					
480	Solar(e+d)	99.2	96.9	97.4	97.4	97.4
	Raman	0.8	3.0	2.4	1.9	2.3
	Fluorescence	0.1	0.1	0.2	0.7	0.3
550	Solar(e+d)	99.6	10.9	< 0.001	0	0
	Raman	0.3	83.3	94.1	93.6	93.4
	Fluorescence	0.008	5.8	5.9	6.4	6.6
660	Solar(e+d)	99.9	0	0	0	0
	Raman	0.04	64.1	40.4	30.4	24.7
	Fluorescence	0.02	35.9	59.6	69.6	75.3

processes (Mobley, 1994) as well as the spectral distribution of irradiance at shorter (blue) wavelengths, which provides a source for both Raman-scattered and fluorescence-generated photons at longer wavelengths. We recall that the simulations with CDOM fluorescence also included chlorophyll-*a* fluorescence, but the latter is unimportant at mesopelagic depths because of the absence of chlorophyll-*a*.

For the simulation representing clear skies and intermediate case of IOPs in the surface mixed layer with $Chl=0.2 \text{ mg m}^{-3}$, Table 2 quantifies the relative contributions to E_0 at selected wavelengths by three categories of photons; solar photons originating from sunlight which have not undergone any transpectral changes, photons produced by the Raman scattering of water molecules, and photons produced by CDOM and chlorophyll-*a* fluorescence. These data demonstrate that solar photons that did not undergo transpectral changes totally dominate the light field at 480 nm throughout the entire water column, Raman scattering is a dominant source of photons at 550 nm within the entire mesopelagic zone, and the contribution of CDOM fluorescence at 660 nm increases with increasing depth and is dominant at depths larger than 500 m.

As these results indicate the profound importance of including inelastic scattering processes in the computation of the mesopelagic light field, in the remainder of this study we restrict our discussion to the results of simulations which include both Raman scattering and fluorescence processes. As illustrated in Fig. 2, both the magnitude and spectral composition of the solar light field at mesopelagic depths vary significantly in response to changes in Chl and hence the IOPs within the surface mixed layer. The magnitude of E_0 at mesopelagic depths does not decrease linearly with an increase in Chl . The values of E_0 at specific mesopelagic depths are reduced typically by ~ 2 orders of magnitude in response to 1 order of magnitude increase in Chl from 0.02 to 0.2 mg m^{-3} but then by ~ 1 order of magnitude with an additional 1 order of magnitude increase in Chl from 0.2 to 2 mg m^{-3} . These responses of the mesopelagic light field to changes in Chl and its vertical distribution throughout the water column are also observed as variation in the spectral composition of E_0 at mesopelagic depths. Fig. 3 illustrates that the different simulation scenarios representing varying levels of Chl in the surface layer have a demonstrable effect on the spectral composition of E_0 within the entire mesopelagic zone including depths as large as 1000 m.

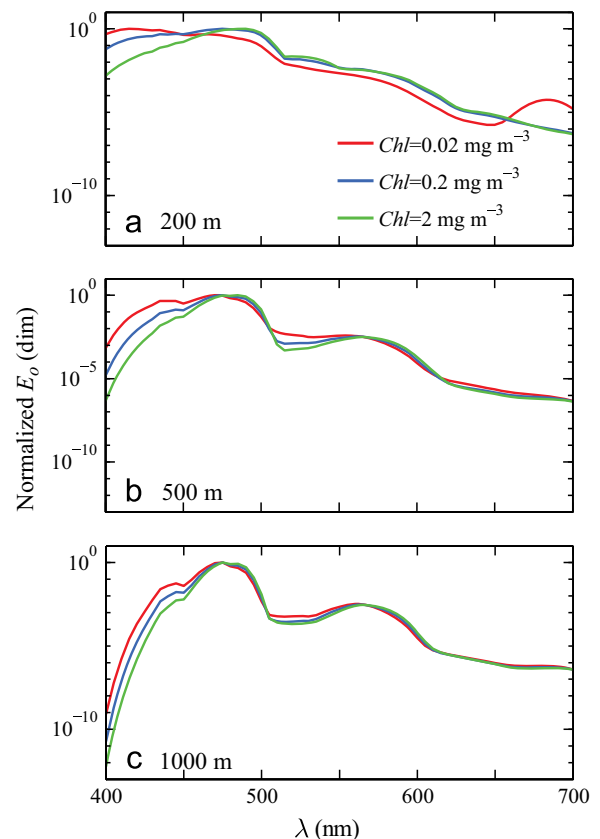


Fig. 3. Model-derived spectra of the scalar irradiance, $E_0(\lambda)$, at 200, 500, and 1000 m depth under clear sky conditions, normalized to equal a value of 1 at the wavelength corresponding to maximum $E_0(\lambda)$, for the three simulation scenarios of varying Chl as indicated. For this and all subsequent figures, the depicted results are for simulations including the presence of both Raman scattering and the fluorescence of CDOM and chlorophyll-*a*.

Previous studies have indicated that light propagation to large depths in clear ocean waters is confined to a narrow spectral region between about 430 nm and 530 nm with a maximum at ~ 475 nm (Boden et al., 1960; Kampa, 1970). Our results support the observations that a dominant feature of the spectral composition of light at mesopelagic depths is a relatively narrow maximum that is generally located within the wavelength range of 430–500 nm (see Figs. 2d–f, 3, and Fig. 4a–c where irradiance is plotted in linear scale). Importantly, however, our results also indicate that a significant number of photons at longer light wavelengths are produced locally at mesopelagic depths by inelastic radiative processes as illustrated in Fig. 2 and Table 2. One important implication of the role of Raman scattering for the spectral composition of mesopelagic light is a distinct secondary maximum of irradiance spectra in the 550–600 nm region with a center wavelength of about 565 nm (see Figs. 2d–f, 3, and 4d–f).

To address the question whether mesopelagic organisms are sensitive to changes in the mesopelagic optical environment arising from changes in surface layer optical properties or sky conditions, it is necessary to quantify how many photons are available within this depth range and determine if these numbers are sufficient for animal vision. Fig. 4d–f depicts the spectra of quantum scalar irradiance E_{0q} obtained by conversion of spectral E_0 into the number of photons per unit area per unit time and per unit wavelength interval. Our simulations for clear sky conditions show that the number of photons undergoes a very large change within the mesopelagic zone, ranging from as many as 10^{13} photons $\text{cm}^{-2} \text{s}^{-1} \text{nm}^{-1}$ in the blue and 10^7 – 10^8 photons $\text{cm}^{-2} \text{s}^{-1} \text{nm}^{-1}$ in the red spectral region at

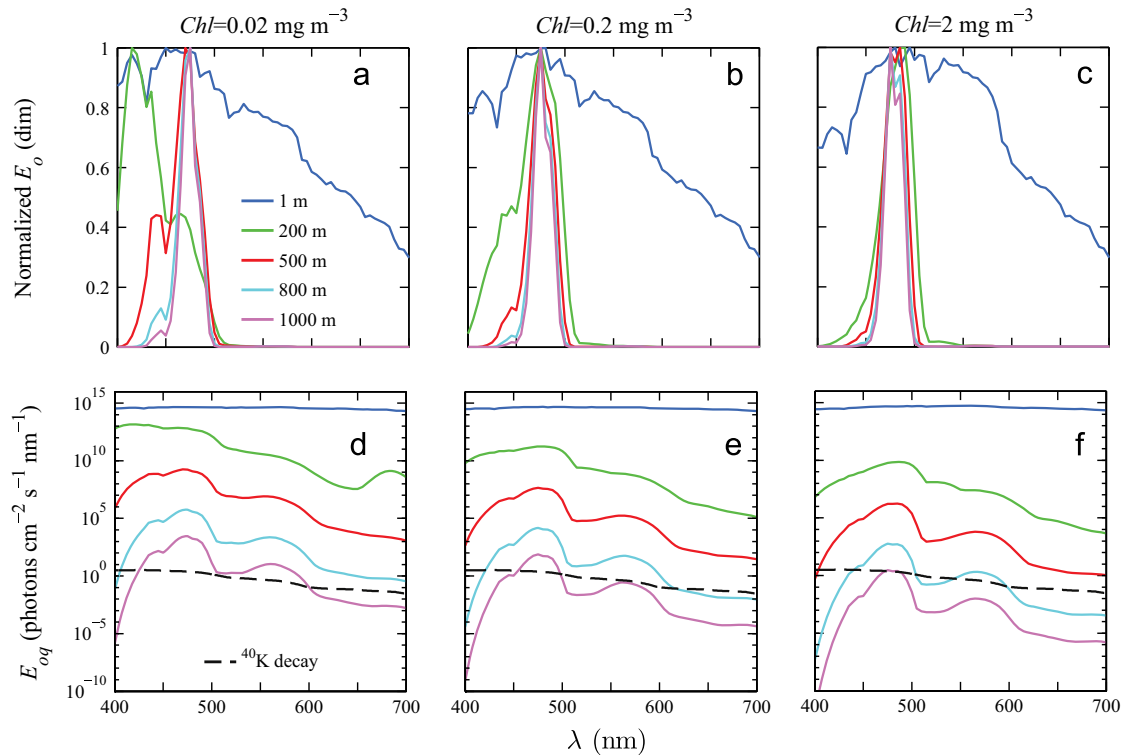


Fig. 4. (a–c) Spectra of the scalar irradiance $E_o(\lambda)$, normalized by the maximum value, at selected depths as indicated for the three simulation scenarios of varying Chl with clear sky conditions. (d–f) Similar to (a–c), but for the unnormalized quantum scalar irradiance $E_{oq}(\lambda)$. For comparison, the spectrum representing decay of potassium isotope ^{40}K is also shown in panels d–f (dashed lines). This spectrum was estimated by Massa (2002) for water salinity of 38.7‰.

$z=200 \text{ m}$ for ultra-oligotrophic surface waters with $Chl=0.02 \text{ mg m}^{-3}$ to less than 100 photons $\text{cm}^{-2} \text{s}^{-1} \text{nm}^{-1}$ in the blue and 1 photon $\text{cm}^{-2} \text{s}^{-1} \text{nm}^{-1}$ in the red at $z=1000 \text{ m}$ for $Chl \geq 0.2 \text{ mg m}^{-3}$. Under overcast sky conditions the number of photons available at specific wavelengths within the mesopelagic zone is naturally reduced, for example 4–5-fold regardless of Chl in our simulations (not shown).

It is also important to emphasize that in addition to solar light (including solar photons that have undergone transpectral changes through inelastic processes), there also exists a low steady optical background within the water column caused by decay of the radioactive isotope ^{40}K contained in sea salt. At typical full oceanic salinities, this decay produces a maximum that exceeds slightly 3 photons $\text{cm}^{-2} \text{s}^{-1} \text{nm}^{-1}$ within the wavelength range 390–450 nm and a decreasing number of photons with increasing wavelength down to 0.03 photons $\text{cm}^{-2} \text{s}^{-1} \text{nm}^{-1}$ at 700 nm (Massa, 2002). For comparison with the quantum scalar irradiance produced by solar photons, Fig. 4d–f includes the counterpart spectrum associated with the decay of ^{40}K . This comparison indicates that the solar irradiance dominates over the ^{40}K -produced light within the majority of the mesopelagic zone for most scenarios considered in this study. The exception is the deepest portion of the mesopelagic zone, i.e., depths larger than about 800 nm, for the red and also partly the green and violet spectral regions. Under ultra-oligotrophic conditions with very low chlorophyll-*a* concentration in the surface ocean ($Chl=0.02 \text{ mg m}^{-3}$), the solar photons dominate over the ^{40}K -produced photons even at a depth of 1000 m across most of the visible spectrum from the blue through the green. In contrast, under eutrophic conditions with high chlorophyll-*a* concentration ($Chl=2 \text{ mg m}^{-3}$), the ^{40}K -produced photons at 1000 m dominate over the solar photons across the entire visible spectrum with the exception of similar values in the vicinity of 480 nm where the solar light exhibits a maximum. Therefore, below 1000 m the

persistent light background is expected to be dominated by the ^{40}K -produced photons. In contrast to persistent light background produced by both solar photons and ^{40}K decay, bioluminescence events are typically intermittent, local, and very rare under natural conditions (e.g., Buskey and Swift, 1990; Priede et al., 2008). Therefore, the rare effects of bioluminescence events on the mesopelagic light field represent a separate problem that is profoundly different and not straightforwardly comparable to persistent background of daylight and ^{40}K decay.

Many deep-sea animals exhibit a maximum visual sensitivity around 480 nm (Macdonald, 1975; Denton, 1990; Frank et al., 2012), but this sensitivity can extend over a relatively broad spectral region from about 460 to 540 nm (Herring, 1996; Warrant and Locket, 2004). Our estimates of E_{oq} at 480 nm for 500 m depth are on the order of 10^9 , 10^7 , and 10^6 photons $\text{cm}^{-2} \text{s}^{-1} \text{nm}^{-1}$ for $Chl=0.02$, 0.2, and 2 mg m^{-3} , respectively (Fig. 4d–f). For a hypothetical sensitivity spectrum of animal visual system estimated on the basis of the study by Frank et al. (2012) with a peak at 480 nm and bandwidth (FWHM) of 100 nm, we estimate that more than 90% of the total number of photons integrated over the entire visible spectrum, namely from about 60 photons $\text{cm}^{-2} \text{s}^{-1}$ for $Chl=2 \text{ mg m}^{-3}$ to 5.7×10^4 photons $\text{cm}^{-2} \text{s}^{-1}$ for $Chl=0.02 \text{ mg m}^{-3}$, are available for vision at the bottom of the mesopelagic zone ($z=1000 \text{ m}$). Therefore, following earlier suggestions that some deep-sea animals can sense extremely low light levels (Denton, 1990; Allen et al., 2010), one can expect that such organisms can perceive changes in the ambient light field throughout the mesopelagic zone caused by variations in Chl and optical properties occurring within the surface mixed layer. Additional supporting evidence for the very good visual abilities of mesopelagic organisms is provided by the experiments of Myslinski et al. (2005), who reported that some crustaceans living at depths of 300–500 m have a visual threshold as low as 10^5 photons $\text{cm}^{-2} \text{s}^{-1} \text{nm}^{-1}$ at 500 nm. This threshold is lower or comparable to E_{oq} at 500 m obtained from our simulations (Fig. 4d–f).

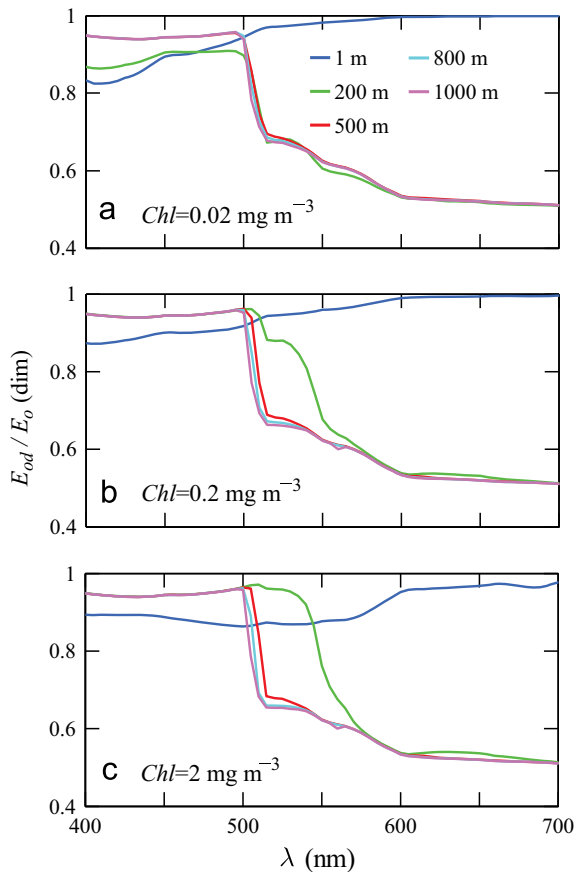


Fig. 5. Spectra representing the ratio of downward scalar irradiance to total scalar irradiance, $E_{od}(\lambda)/E_o(\lambda)$, at selected depths as indicated for the three simulation scenarios of varying Chl with clear sky conditions.

The total spectral scalar irradiance, E_o , can be partitioned into the contributions of the downwelling and upwelling light, which are quantified respectively by the downward spectral scalar irradiance, E_{od} , and the upward spectral scalar irradiance, E_{ou} (e.g., Mobley, 1994). This partitioning provides a means for characterizing the proportions of downwelling and upwelling light in the total light field in terms of the ratios E_{od}/E_o and E_{ou}/E_o ($\equiv 1 - E_{od}/E_o$). Fig. 5 depicts the spectra of the ratio E_{od}/E_o at selected depths as obtained from the simulations under clear sky conditions for the three Chl scenarios. In general, the variations in this ratio associated with different Chl are manifested within the surface layer and at the top of mesopelagic zone, and reflect the differences in the IOPs of mixed-layer water among the three scenarios. These differences mostly vanish at deeper depths within the mesopelagic zone. In this depth region, downwelling light dominates within the blue spectral region (i.e., 400–500 nm) with values of E_{od}/E_o exceeding 0.85, reflecting the predominant contribution of downward traveling solar photons that did not undergo transpectral changes (Table 2). The contribution of E_{od} to E_o sharply decreases from 500 nm to 700 nm until reaching nearly the same level as E_{ou} ($E_{od}/E_o \approx 0.5$), consistent with an increasing role of photons originating from inelastic processes.

Comparisons of irradiance simulated in our study with previous measurements at mesopelagic depths are satisfactory. Specifically, we can compare measurements of downward plane irradiance, E_d , made by Kampa (1970) in clear ocean waters off Tenerife (the Canary Islands) with our simulations. The measured E_d at 474 nm at mesopelagic depths of 290, 342, 480, and 615 m were respectively 4.9×10^{-4} , 1.2×10^{-4} , 4.7×10^{-6} , and $1.1 \times 10^{-7} \text{ W m}^{-2} \text{ nm}^{-1}$. These values are between two scenarios

of our simulations of clear ocean waters under clear sky conditions, namely $Chl=0.02 \text{ mg m}^{-3}$ and 0.2 mg m^{-3} . The measured values also fall between two scenarios of our simulations characterized by clear and overcast skies for ultra-oligotrophic waters with $Chl=0.02 \text{ mg m}^{-3}$. These comparisons are consistent with the assessment of very high clarity of waters in which the measurements of Kampa (1970) were made. The attenuation coefficients for downward irradiance reported in that study were similar to those defined by Jerlov (1976) for the clearest ocean waters of Type I.

We can also compare our simulations of quantum downward plane irradiance, E_{dq} , with measurements at mesopelagic depths reported in Myslinski et al. (2005). These measurements were taken for E_{dq} at 480 nm during four summer seasons in Oceanographer Canyon on the southwest edge of Georges Bank. Although the clarity of surface waters is not reported in Myslinski et al. (2005), we expect that during those measurements the surface waters contained relatively high chlorophyll-*a* concentration. From the NASA SeaWiFS Bio-optical Archive and Storage System (SeaBASS) database (Werdell and Bailey, 2002; Werdell et al., 2003), we identified Chl measurements taken in this region during October with Chl exceeding 2 mg m^{-3} within the top 30 m of surface layer (data collected by R. Morrison and H. Sosik), which is above the highest value used in our simulations. The minimum value of $E_{dq}(480)$ which was measured by Myslinski et al. (2005) was $10^4 \text{ photons cm}^{-2} \text{ s}^{-1} \text{ nm}^{-1}$, and this value was observed within the depth range from about 400 to 650 m during different experiments. In our simulations for $Chl=2 \text{ mg m}^{-3}$, the value $E_{dq}(480)=10^4 \text{ photons cm}^{-2} \text{ s}^{-1} \text{ nm}^{-1}$ is observed at about 680 m under clear skies and 620 m for the overcast scenario. These depths are consistent with a subset of measurements by Myslinski et al. (2005) corresponding to the deepest penetration of light. These comparison results are reasonable because most measurements by Myslinski et al. (2005) were likely made with $Chl > 2 \text{ mg m}^{-3}$ resulting in reduced penetration of light into the mesopelagic zone compared with the case $Chl=2 \text{ mg m}^{-3}$.

3.2. Radiance field

Whereas the scalar irradiances E_o , E_{od} , and E_{ou} quantify the integrated amount of radiant power per unit area over all directions, all downwelling directions, or all upwelling directions of light propagation, these quantities do not provide a detailed description of the directional structure of the light field. Full information on the angular distribution of light at a given depth is provided by the spectral radiance, $L(z, \theta, \phi, \lambda)$. For practical reasons, we limit the presentation of $L(z, \theta, \phi, \lambda)$ data to the one intermediate case of $Chl=0.2 \text{ mg m}^{-3}$, three example wavelengths (480, 550, and 660 nm), several depths (1, 200, 300, 400, 500, 800, and 1000 m), and two azimuthal planes that are orthogonal to one another, specifically the principal solar plane ($\phi=0^\circ$ and 180°) and perpendicular plane ($\phi=90^\circ$ and 270°). Fig. 6 depicts the distributions of downwelling radiance, $L_d(z, \theta_n, \phi, \lambda)$, and upwelling radiance, $L_u(z, \theta_z, \phi, \lambda)$, for these two azimuthal planes as a function of angle θ representing the direction of photon travel relative to the vertical. Under clear sky conditions when the sun is not at zenith (as is the case for the simulations in Fig. 6), a maximum of L_d at sufficiently small depths in the ocean will occur within the principal solar plane at some negative value of θ_n consistent with the direction of refracted solar rays underwater. This feature is indeed clearly seen in Fig. 6 for the calculated distributions of L_d at 1 m depth. In contrast, for all other cases presented in Fig. 6 including all L_d data for mesopelagic depths, all L_u data, and all data for the plane perpendicular to the solar principal plane, the radiance distributions show no such feature with direct relation to the position of sun in the sky.

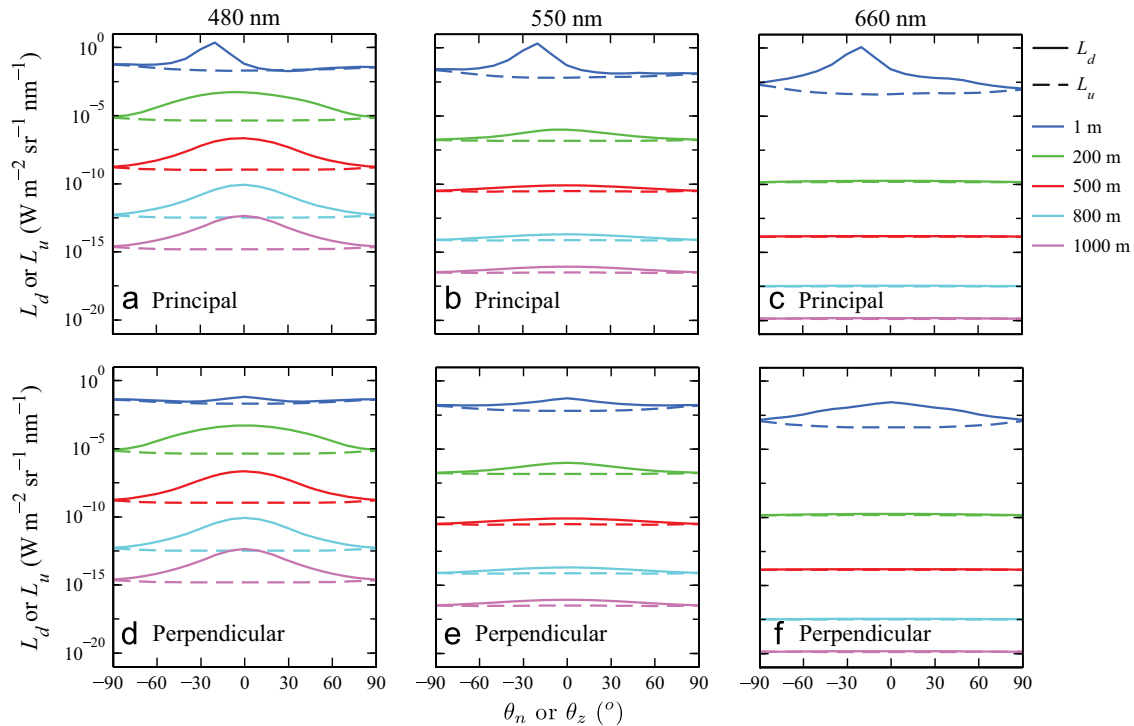


Fig. 6. Magnitudes of downwelling, $L_d(\theta_n, \phi, \lambda)$, and upwelling, $L_u(\theta_z, \phi, \lambda)$, spectral radiance at selected depths and light wavelengths as a function of vertical angle for the simulation representing $Chl=0.2 \text{ mg m}^{-3}$ and clear sky conditions. Results are illustrated for two azimuthal planes, the principal solar plane (a–c, half plane $\phi=0^\circ$ contains the sun and $\phi=180^\circ$ represents the opposite half plane) and the plane perpendicular to the solar plane (d–f, $\phi=90^\circ$ and 270°). Downwelling radiance is depicted as a function of nadir angle θ_n , upwelling radiance as a function of zenith angle θ_z , with values representing the direction of photon travel (see text for further details).

At mesopelagic depths L_d in the blue spectral region shows a well pronounced maximum for $\theta_n=0^\circ$ in both azimuthal planes (Fig. 6a and d). This dependence of L_d on θ_n decreases with increasing light wavelength (Fig. 6b, c, e, and f), which results from the increased contributions of inelastic processes. The dependence of L_u on θ_z is relatively weak for all wavelengths, and in consequence the angular patterns for L_d and L_u are very similar in the red spectral region. Fig. 6 also illustrates the differences between L_d and L_u in terms of magnitude. Whereas the values of L_d and L_u naturally converge at horizontal directions, for other directions L_d is generally higher than L_u . These differences are largest in the blue and smallest in the red spectral region. For example, in the blue spectral region at $z=200 \text{ m}$, $L_d(200 \text{ m}, 0^\circ, \phi, 480 \text{ nm})$ is $\sim 5.1 \times 10^{-4} \text{ W m}^{-2} \text{ sr}^{-1} \text{ nm}^{-1}$ and $L_u(200 \text{ m}, 0^\circ, \phi, 480 \text{ nm})$ is $\sim 4.3 \times 10^{-6} \text{ W m}^{-2} \text{ sr}^{-1} \text{ nm}^{-1}$. At $z=1000 \text{ m}$, $L_d(1000 \text{ m}, 0^\circ, \phi, 480 \text{ nm})$ is $\sim 4.4 \times 10^{-13} \text{ W m}^{-2} \text{ sr}^{-1} \text{ nm}^{-1}$ and $L_u(1000 \text{ m}, 0^\circ, \phi, 480 \text{ nm})$ is $\sim 1.6 \times 10^{-15} \text{ W m}^{-2} \text{ sr}^{-1} \text{ nm}^{-1}$. For most wavelengths, both L_d and L_u generally drop by ~ 9 – 10 orders of magnitude between $z=200 \text{ m}$ and 1000 m . However, for any specific wavelength the relative difference between $L_d(z, \theta_n, \phi, \lambda)$ and $L_u(z, \theta_z, \phi, \lambda)$ remains about the same at various mesopelagic depths, e.g., ~ 2 orders of magnitude difference at 480 nm , ~ 1 order of magnitude at 550 nm , and almost no difference at 660 nm . This result implies that the angular distribution of radiance is fairly stable within the mesopelagic zone and tends toward an isotropic distribution at longer wavelengths of the visible spectrum, albeit not achieving such distribution.

Further insight into the variations in the angular distribution of radiance is provided in Fig. 7, which depicts $L(z, \theta, \phi, \lambda)$ in polar coordinates after normalization by its maximum value (hereafter referred to as the L shape). These results were derived from the data presented in Fig. 6, but also include the L shapes for two additional depths of 300 m and 400 m . It is also important to note that the true L shapes in the ocean for light wavelengths where Raman scattering plays a significant role (i.e., 550 nm and 660 nm

in Fig. 7) are expected to be somewhat different from those obtained from our simulations. This is because, for the sake of computational simplicity, the Hydrolight model assumes an isotropic Raman scattering phase function rather than a more accurate moderately anisotropic function. This limitation is largely irrelevant for the blue wavelengths (i.e., 480 nm in Fig. 7) because of the negligible contributions of inelastic processes. Although it can have larger influence at longer wavelengths (i.e., the L shape may differ somewhat more from the isotropic distribution than suggested by our simulations), the main conclusions drawn from Fig. 7 are expected to be qualitatively valid.

The L shapes presented in Fig. 7 show that the angular distribution of light in the mesopelagic zone is dramatically different at different wavelengths. Downwelling photons dominate the radiance field at 480 nm , in contrast to 660 nm where L_d and L_u have similar contributions. This approach towards an isotropic light field at longer wavelengths is a natural consequence of the increasing predominance of photons originating from the inelastic processes of Raman scattering and CDOM fluorescence, which are both represented in the simulations as isotropic phase functions for the emission wavelengths. Further examination of the data suggests that the L shapes at 550 nm and 660 nm remain nearly unchanged throughout the mesopelagic zone below 300 – 400 m , implying that the nearly-asymptotic light field has been reached (see also Berwald et al., 1998). Importantly, however, the L shape at 480 nm continues to exhibit a conspicuous change with depth throughout the entire water column down to 1000 m , implying that the asymptotic light field is not reached within the mesopelagic zone within the blue spectral region. However, because the L shape at 480 nm changes relatively slowly with depth, for practical purposes the light field in the blue can be assumed to be nearly-asymptotic below 300 – 400 m . In general, our results highlight the importance of the contributions from inelastic processes to establish the nearly-asymptotic field in the ocean. This conclusion was further verified in the simulations

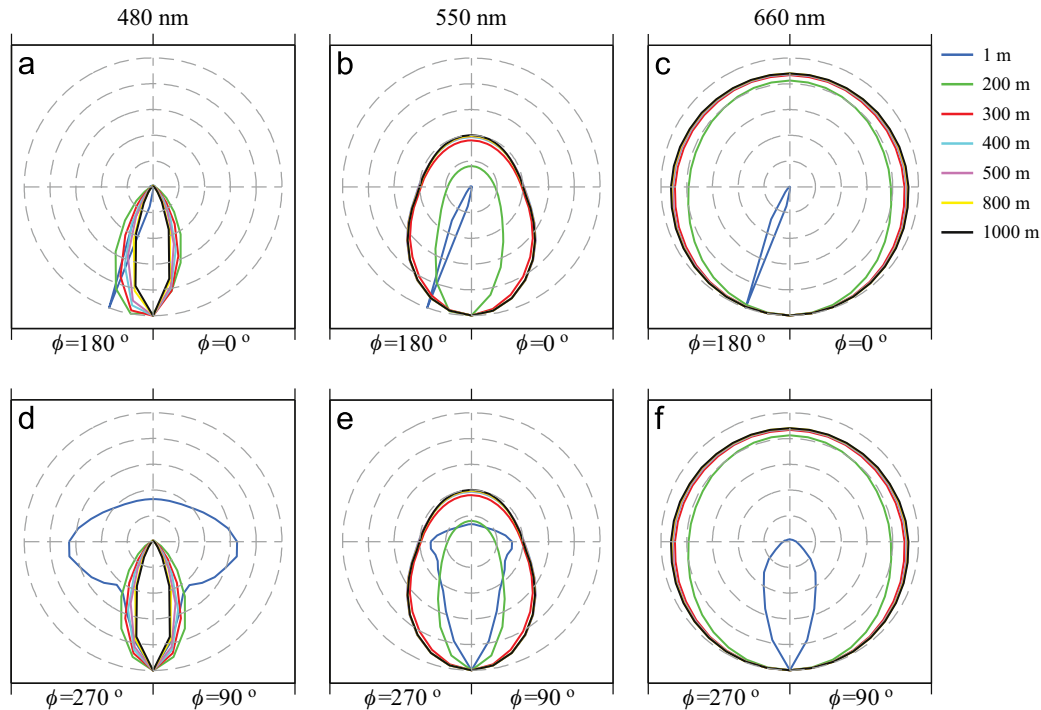


Fig. 7. Similar to Fig. 6, but using a polar diagram to depict the relative shape of the full angular distribution of radiance $L(\theta, \phi, \lambda)$ at selected depths and light wavelengths. Each distribution has been normalized to equal a value of 1 at the maximum radiance, represented by the radial coordinate (gray dashed lines indicate scale 0–1 with 0 at the center) with direction θ indicated by the angular coordinate. Data from two additional depths (300 and 400 m) have been added to better illustrate vertical changes.

without inelastic processes, in which the nearly-asymptotic light field was never obtained. These findings regarding the necessary role of inelastic processes for reaching the nearly-asymptotic light field modify the conclusions from early studies of asymptotic light field which ignored inelastic processes (Preisendorfer, 1959; Høgerslev and Zaneveld, 1977), but are generally consistent with a more recent study of Berwald et al. (1998).

The angular distribution of light in the mesopelagic zone is important for camouflage strategies and the design of visual systems for animals inhabiting this region of the ocean. Many mesopelagic animals have upward looking eyes that utilize photons around 480 nm for object detection (Denton, 1990; Herring, 1996; Warrant and Locket, 2004). Fig. 7a and d indicates that about ~85% of downwelling radiance at 480 nm is concentrated within the directions of $\pm 15^\circ$ from the nadir, which is consistent with the angular range corresponding to the highest vision sensitivity of many deep-sea organisms (Warrant and Locket, 2004). It is also important to recognize from our simulations that there also appear to be sufficient numbers of photons available for vision at longer wavelengths such as 550 nm and 660 nm, especially within the upper portion of the mesopelagic zone. Organisms living at these depths can have color vision (Johnsen and Sosik, 2004) and can detect objects from all directions (Warrant and Locket, 2004).

3.3. Apparent optical properties

3.3.1. Irradiance reflectance

Experimental studies commonly characterize the downwelling and upwelling flow of radiant energy within a water body through concomitant measurements of the spectral downward plane irradiance, E_d , and the spectral upward plane irradiance, E_u (e.g., Mobley, 1994). The ratio E_u/E_d is an apparent optical property (AOP) of the water body and is referred to as the spectral irradiance reflectance, R . This reflectance is a measure of the

proportion between the spectral upward and downward light incident on a horizontal plane at any given depth in the ocean.

Fig. 8a–c depicts the spectra of R at selected depths obtained from the simulations under clear sky conditions for the three scenarios of *Chl*. These spectra differ greatly between near-surface and mesopelagic depths, with the largest differences occurring within the long-wavelength part of the spectrum for $\lambda > 500$ nm. At mesopelagic depths the values of R in the red spectral region exceed 0.9, a value 2–3 orders of magnitude higher than near-surface values. This results from the dominant effect of inelastic processes on the light field at mesopelagic depths. In contrast, in the blue spectral region where the role of inelastic processes is very small or negligible, the values of R at mesopelagic depths are low (typically < 0.03) and smaller compared with the near-surface ocean. Regardless of *Chl* and IOPs within the surface layer, the magnitude and spectral shape of R remain very similar throughout most of the mesopelagic zone for depths larger than about 300 m (Fig. 8). In the upper portion of the mesopelagic zone, R can differ from the values at deeper depths; for example, in the spectral range from about 500 to 580 nm for scenarios with higher *Chl* (Fig. 8b and c).

The spectral distribution of R (Fig. 8a–c) and its stability throughout much of the mesopelagic zone irrespective of overlying surface conditions (Fig. 8d) may have important implications to vision and crypsis of mesopelagic animals. In the blue spectral region where R is relatively low, mesopelagic animals tend to utilize mostly the downwelling light for vision (Herring, 1996; Warrant and Locket, 2004; Johnsen, 2005). For longer wavelengths, at which inelastic processes produce high values of R and a more uniform angular distribution of light, the photon numbers may be sufficient for vision only within the upper portion of the mesopelagic zone. In addition, the uniform vertical profiles of spectral values of R at depths exceeding 300 m can play an important role in the crypsis of mesopelagic animals as cryptic abilities depend largely on the differences between the background reflectance of the ambient light field and the body

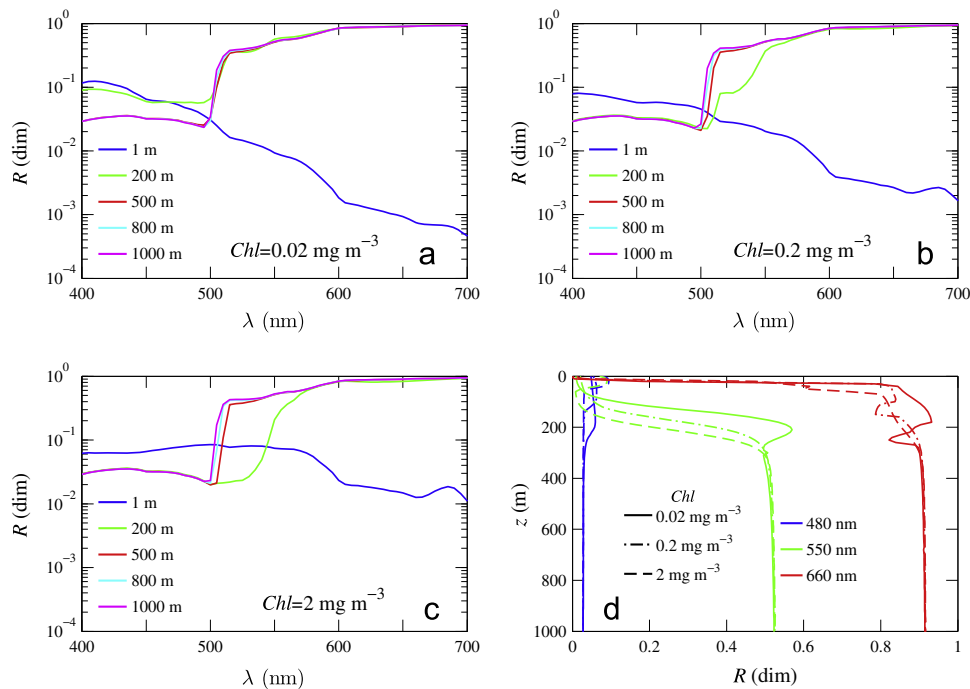


Fig. 8. (a–c) Spectra of the irradiance reflectance $R(\lambda) = E_u(\lambda)/E_d(\lambda)$ at selected depths as indicated for the three simulation scenarios of varying Chl with clear sky conditions. (d) Corresponding vertical profiles of $R(\lambda)$ at selected light wavelengths as indicated.

reflectance of the organisms. Mesopelagic organisms have developed various strategies for crypsis such as production of bioluminescence to match the optical background, a flattened body to form silvering, and different coloration (Herring, 1996; Johnsen and Sosik, 2004; Warrant and Locket, 2004; Johnsen, 2005). These strategies can be utilized in conjunction with vertical migration within the water column.

3.3.2. Average cosines of the light field

The average cosines are additional AOPs that provide a simple means to characterize the angular distribution of light on the basis of plane and scalar irradiances (Mobley, 1994; Berwald et al., 1998). These quantities are defined as

$$\bar{\mu} = \frac{E_d - E_u}{E_{od} + E_{ou}}; \quad \bar{\mu}_d = \frac{E_d}{E_{od}}; \quad \text{and} \quad \bar{\mu}_u = \frac{E_u}{E_{ou}} \quad (7)$$

where $\bar{\mu}$ is the average cosine for total light field, $\bar{\mu}_d$ the average cosine for the downwelling light field, and $\bar{\mu}_u$ the average cosine for the upwelling light field.

Fig. 9 illustrates the average cosines computed from the simulations for the case of clear skies and $Chl = 0.2 \text{ mg m}^{-3}$. The spectra of $\bar{\mu}$ and $\bar{\mu}_d$ at mesopelagic depths are very different from the spectra at the near-surface depth (Fig. 9a and b). The differences are much smaller for the spectra of $\bar{\mu}_u$ (Fig. 9c). The spectral pattern of $\bar{\mu}$ at mesopelagic depths is characterized by relatively large values (approximately within the range 0.75–0.8) in the blue spectral region, an abrupt decrease near 500 nm, and a further gradual decrease to values close to zero (< 0.02) at the long-wavelength end of the visible spectrum. This pattern is consistent with the results discussed above for the mesopelagic radiance field and irradiance reflectance. The light field in the blue is dominated by downward propagation around the vertical direction, and consists of solar photons that have not undergone any transpectral changes. In contrast, the light field in the red becomes more uniform owing to inelastic radiative processes.

The average cosine of the downwelling light field, $\bar{\mu}_d$, exhibits a similar spectral pattern to $\bar{\mu}$ (Fig. 9b). One noticeable difference is a somewhat higher $\bar{\mu}_d$ compared with $\bar{\mu}$ in the blue spectral region.

In the red spectral region, $\bar{\mu}_d$ approaches the value of 0.5, which indicates that the angular distribution of downwelling light is nearly uniform. In contrast to $\bar{\mu}$ and $\bar{\mu}_d$, the average cosine of the upwelling light field, $\bar{\mu}_u$, shows weak spectral dependence (Fig. 9c). The values of $\bar{\mu}_u$ at mesopelagic depths are somewhat higher across the entire spectrum compared with near-surface values. The spectral values of $\bar{\mu}_u$ are relatively close to 0.5 at all wavelengths but more so in the red part of the spectrum, indicating a nearly uniform angular distribution of upwelling light.

The angular distributions of downwelling and upwelling light exhibit different sensitivity to the presence of inelastic radiative processes. With no inelastic processes included in the simulations, $\bar{\mu}$ and $\bar{\mu}_d$ at mesopelagic depths are very different from the data presented in Fig. 9 and have a spectrum similar to that at the ocean surface (not shown). In contrast, $\bar{\mu}_u$ in the absence of inelastic processes exhibits a very similar pattern to that obtained in the presence of inelastic processes and depicted in Fig. 9c. These results indicate that whereas the inelastic processes have a significant effect on the angular distribution of downwelling light, especially at wavelengths $> 500 \text{ nm}$, their influence on modifying the angular distribution of upwelling light is small.

The vertical profiles of all average cosines tend to reach nearly constant values at mesopelagic depths below 300–400 m (Fig. 9d). As the average cosines serve as simple proxies for the angular distribution of light, these observations are in agreement with the results describing the full angular distribution of radiance at several discrete depths presented in Fig. 7. Overall, our simulations suggest the existence of a nearly-asymptotic light field throughout much of the mesopelagic zone, and are in accordance with the results of previous radiative transfer simulations which included Raman scattering but only extended to depths of 400–600 m (Berwald et al., 1998). It must be noted that $\bar{\mu}$ and $\bar{\mu}_d$ in the blue spectral region can still undergo a small noticeable change with depth throughout the mesopelagic zone (see the curves for 480 nm in Fig. 9d). This result is consistent with the conclusions drawn from Fig. 7a and d and the earlier suggestion that the assumption of nearly-asymptotic light field in the blue can be reasonable.

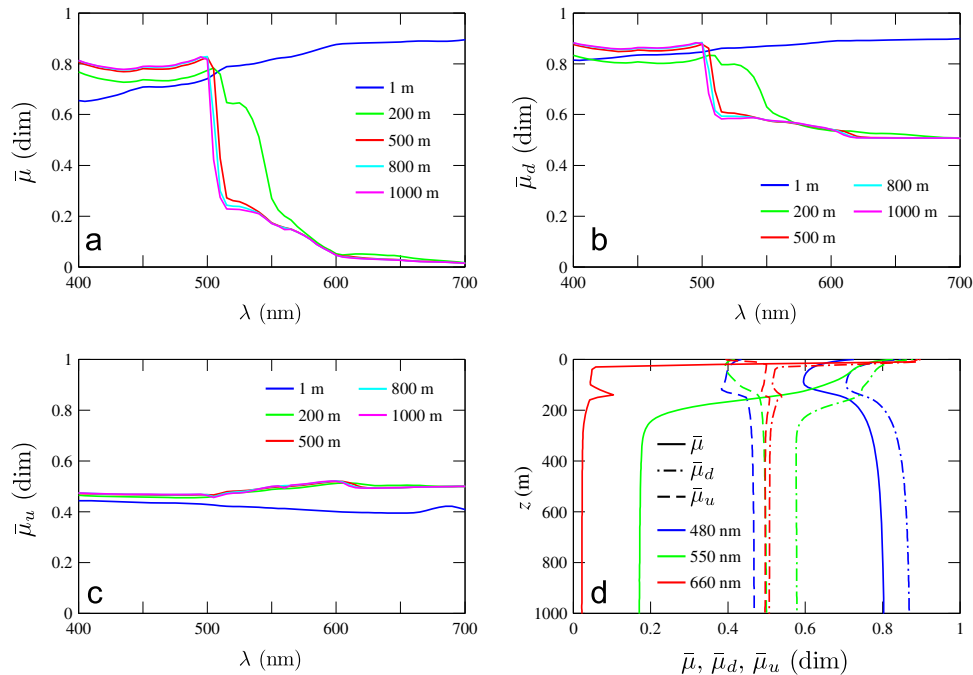


Fig. 9. Computed values of the average cosines for light field from the simulation scenario of $Chl=0.2 \text{ mg m}^{-3}$ and clear sky conditions. (a–c) Spectra of the average cosine for total light field, $\bar{\mu}(\lambda)$, downwelling light field, $\bar{\mu}_d(\lambda)$, and upwelling light field, $\bar{\mu}_u(\lambda)$, at selected depths as indicated. (d) Corresponding vertical profiles of each average cosine quantity at selected light wavelengths as indicated.

3.3.3. Diffuse attenuation coefficients

The vertical diffuse attenuation coefficients (the common symbol K) are AOPs that characterize the attenuation of radiance and irradiance with depth in a water body (Mobley, 1994). The spectra of three diffuse attenuation coefficients, K_d for downward plane irradiance, K_u for upward plane irradiance, and K_{Lu} for upwelling radiance for the vertical direction of light propagation (i.e., L_u for $\theta_z=0^\circ$) are illustrated in Fig. 10a–c. Fig. 10d shows the vertical profiles of these coefficients at three selected light wavelengths, and additionally shows the profiles for the diffuse attenuation coefficient of scalar irradiance, K_o . These results were obtained from simulations for $Chl=0.2 \text{ mg m}^{-3}$ and clear sky conditions.

The spectra of K -coefficients differ between the near-surface and mesopelagic depths (Fig. 10a–c). For $\lambda > 500 \text{ nm}$, the differences increase greatly in concert with the increasing contribution of inelastic processes to the mesopelagic light field. Because of these contributions, the K -coefficients in the green and red spectral regions within the mesopelagic zone are reduced to an extent well below the values of the absorption coefficient by pure water. This effect produces a relatively flat spectral shape of K -coefficients across the entire visible spectrum at mesopelagic depths. Because photons in the green and red spectral regions are produced locally through inelastic processes that originate from excitation by photons in the blue spectral region, the deep-sea spectra of K -coefficients are not perfectly flat but exhibit some undulations linked to the spectral shape of light in the blue and the spectral shifts between the excitation and emission wavelengths. These results are consistent with previous predictions of K -coefficients for the nearly-asymptotic light field in the presence of inelastic processes (Gordon and Xu, 1996; Berwald et al., 1998).

At depths below $\sim 400 \text{ m}$, the coefficients K_o , K_d , K_u , and K_{Lu} at any specific wavelength are approximately the same (Fig. 10d). Such convergence of the different K -coefficients on the same value suggests that light is attenuated with depth at the same rate at various directions of propagation. This result is consistent with the conclusion that the angular distribution of light remains

approximately constant below $\sim 400 \text{ m}$, which was discussed previously in relation to the radiance field and average cosines. In addition, the simulated values of K_d are comparable to measurements made by Kampa (1970) in clear Atlantic waters off Tenerife, which were mentioned earlier within the context of irradiance. For example, the values of K_d at 480 nm estimated from the measurements at mesopelagic depths between about $200\text{--}600 \text{ m}$ range between 0.023 and 0.028 m^{-1} . The corresponding values from our simulations are $0.027\text{--}0.028 \text{ m}^{-1}$. Interestingly, the measurements of Kampa (1970) at the green waveband of 533 nm appear to provide unique experimental evidence of the effect of inelastic processes in this spectral region at mesopelagic depths. Whereas $K_d(533)$ derived from measurements within the epipelagic zone (depth range $80\text{--}190 \text{ m}$) was 0.038 m^{-1} , the $K_d(533)$ values dropped significantly to $0.025\text{--}0.026 \text{ m}^{-1}$ at mesopelagic depths, which is consistent with the pattern observed in our simulations and attributed to inelastic processes.

3.4. Nearly-asymptotic light field

The results describing the angular distribution of radiance (Fig. 7), the average cosines (Fig. 9), and K -coefficients (Fig. 10) all suggest that the assumption of nearly-asymptotic light field below a depth of about 400 m is reasonable for the simulations representing $Chl=0.2 \text{ mg m}^{-3}$. The inspection of vertical profiles of the average cosine of the light field, $\bar{\mu}$, and the diffuse attenuation coefficient of scalar irradiance, K_o , for the three Chl cases examined in this study also supports the notion that the mesopelagic light field approximates the asymptotic regime whose properties do not depend on the IOPs in the surface layer (Fig. 11a and b). For any specific light wavelength, the $\bar{\mu}$ and K_o profiles converge at depths below $400\text{--}500 \text{ m}$ for the three Chl cases examined. Although the degree of convergence is somewhat weaker for K_o in the red spectral region, the values of K_o are constrained within a very small range for all light wavelengths and Chl cases considered. The vertical profiles of other AOPs including irradiance reflectance (see Fig. 8d) similarly exhibit this feature

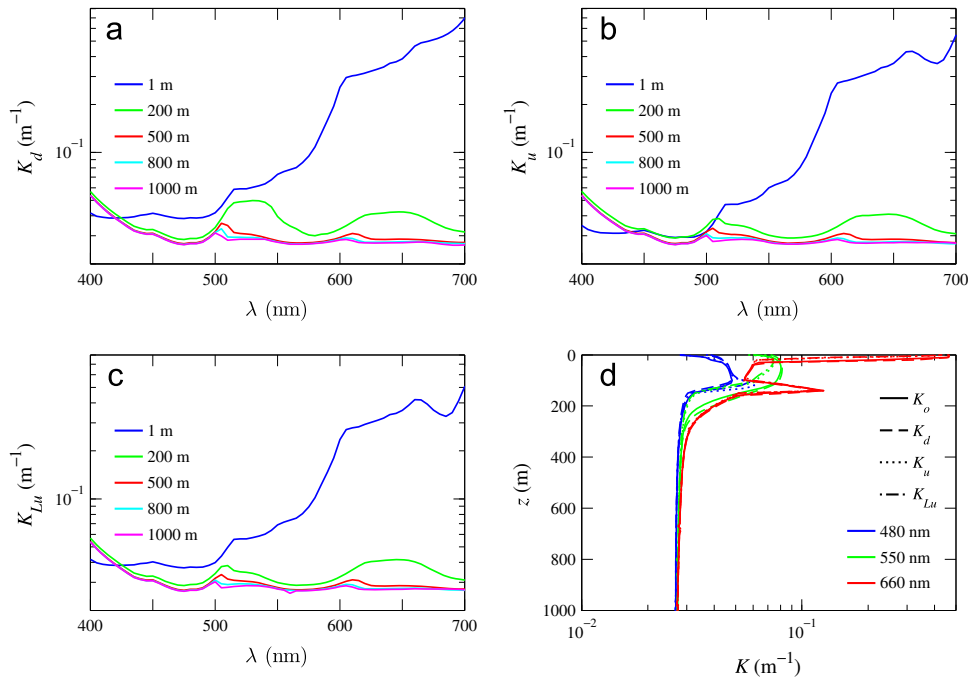


Fig. 10. Similar to Fig. 9, but for the spectral diffuse attenuation coefficients of downwelling plane irradiance, $K_d(\lambda)$, upwelling plane irradiance, $K_u(\lambda)$, and upwelling radiance in the vertical direction, $K_{Lu}(\lambda)$. The vertical profile of the spectral diffuse attenuation coefficient of scalar irradiance, $K_o(\lambda)$, is additionally illustrated in (d).

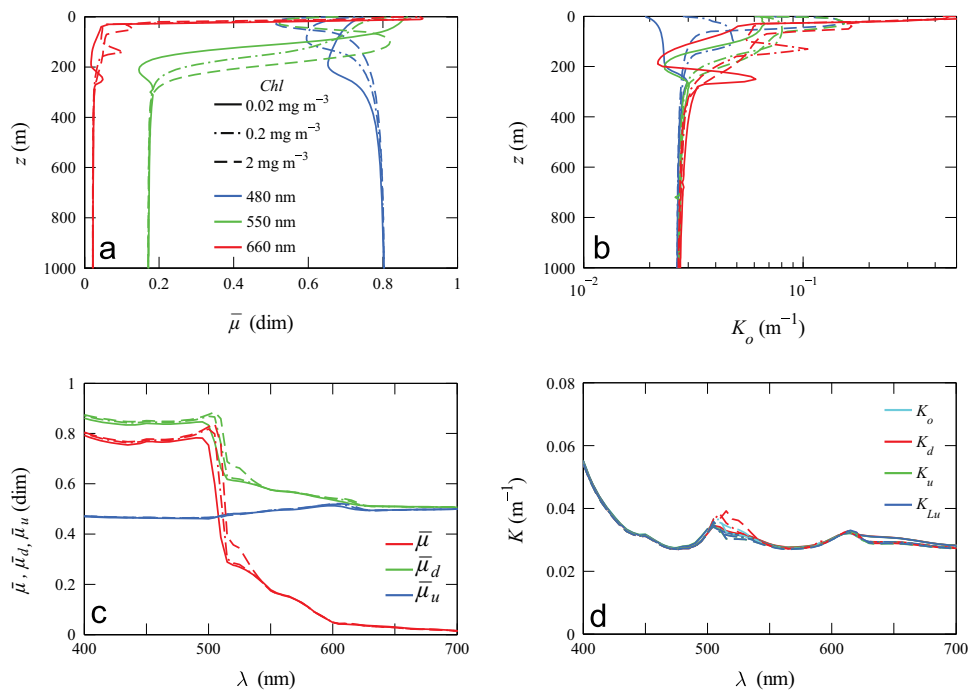


Fig. 11. (a–b) Vertical profiles of average cosine $\bar{\mu}(\lambda)$ and diffuse attenuation coefficient $K_o(\lambda)$ at selected light wavelengths as indicated for the three simulations of varying Chl with clear sky conditions. (c–d) Spectra of the average cosines and diffuse attenuation coefficients at 400 m depth for these three simulations. Descriptions of the various average cosines and diffuse attenuation coefficients are provided in the text and in Figs. 9 and 10.

of convergence on approximately the same value (at a given wavelength) which is nearly independent of depth below about 400 m regardless of Chl and IOPs in the surface layer.

Considering the particular importance of the middle portion of the mesopelagic zone where the nearly-asymptotic regime begins, the spectra of three average cosines, $\bar{\mu}$, $\bar{\mu}_d$, and $\bar{\mu}_u$, and four attenuation coefficients, K_o , K_d , K_u , and K_{Lu} , at 400 m depth are shown in Fig. 11c and d. These results were obtained from

simulations for the three Chl cases under clear skies. At the depth of 400 m, all the presented AOPs become weakly sensitive to large changes in Chl within the surface ocean. This result will hold for Chl higher than the largest value of 2 mg m^{-3} used in our simulations, and is consistent with the previous study by Berwald et al. (1998) who considered Chl as high as 5 mg m^{-3} . We also note that variations in the boundary conditions at the ocean surface exert a very weak influence on the nearly-asymptotic characteristics of the

mesopelagic light field as verified in this study by comparisons of simulations for clear and overcast skies (not shown).

It is important to emphasize that the necessary criteria for the asymptotic light field are generally best satisfied within the green and red portions of the spectrum. For shorter wavelengths between 400 and 500 nm the angular distribution of radiance and AOPs can undergo minor changes with depth throughout most of mesopelagic zone even though the inherent optical properties for this layer were assumed constant in our simulations (e.g., Fig. 7). The K -coefficients in the red also exhibit small vertical variation at large mesopelagic depths (Fig. 11b). Nevertheless, the general assumption of the existence of a nearly-asymptotic light field below a depth of 400 m, or more conservatively 500 m, appears to provide a reasonable approximation under most circumstances. This finding has significant practical implications as it allows the calculation of light field characteristics within the entire deeper portion of the mesopelagic zone from vertical profile measurements of irradiance or radiance which extend down only to 400–500 m. This is an important aspect in view of the extremely low light levels in the lower mesopelagic zone and the associated high demands on the sensitivity of deep-sea radiometers. As noted earlier, direct measurements of ambient light at mesopelagic depths are very rare. Recently, Myslinski et al. (2005) used a low-light radiometer to measure the quantum downward irradiance at 480 nm at depths extending to 400–650 m where the measured irradiance was as low as 10^4 photons $\text{cm}^{-2} \text{s}^{-1} \text{nm}^{-1}$. By using the measured attenuation coefficient (and implicitly assuming the asymptotic light field and constant IOPs) these investigators extrapolated the irradiance measurements to depths as large as 800 m.

Given the potential applicability of such extrapolation through the nearly-asymptotic regime within the deep portion of the mesopelagic zone, it is important to know typical magnitudes of irradiance and radiance at the top of the nearly-asymptotic light field. These magnitudes define a minimum radiometric sensitivity required for mesopelagic measurements. Fig. 12 depicts three irradiances (E_o , E_d , and E_u) and two radiances (downwelling vertical radiance L_d and upwelling vertical radiance L_u) at a depth

of 400 m as obtained from our simulations for clear sky conditions and $\text{Chl}=0.2 \text{ mg m}^{-3}$. Compared with this Chl scenario, the magnitude of radiometric quantities increases by ~ 2 orders of magnitude for a very low Chl of 0.02 mg m^{-3} and decreases by ~ 1 order of magnitude for higher Chl of 2 mg m^{-3} (not shown). For overcast sky conditions the irradiance and radiance values decrease 4–5-fold compared with clear sky conditions (not shown). In addition, solar zenith angles other than that used in our simulations (30°) would also naturally influence the incident irradiance at the ocean surface and consequently the magnitude of radiometric quantities underwater. This analysis suggests that in order to conduct measurements at 400 m depth under most environmental conditions, including conditions less favorable than those represented by Fig. 12, a “mesopelagic” radiometer must provide a capability to detect light levels lower by a few orders of magnitude compared with those shown in Fig. 12. It is also important to recall that whereas these considerations are relevant to the ambient solar light, the mesopelagic optical environment can also include contributions by decay of the potassium isotope ^{40}K (Massa, 2002) and bioluminescent glow and flashes (Clarke and Kelly, 1965; Boden and Kampa, 1974; Haddock et al., 2010). Although bioluminescence is generally rare under natural conditions, the mechanical disturbance of water such as the deployment of instruments can potentially stimulate large amount of bioluminescent flashes (Buskey and Swift, 1990; Priede et al., 2008).

4. Conclusions

We examined the magnitude, spectral composition, and angular distribution of the solar ambient light field for the entire visible spectrum within the entire mesopelagic zone of the ocean (depth range 200–1000 m) using radiative transfer simulations. The simulations demonstrate the critical need to include inelastic radiative processes, especially Raman scattering by water molecules and CDOM fluorescence, in modeling and interpretation of the light field at mesopelagic depths. Although these processes have a small or

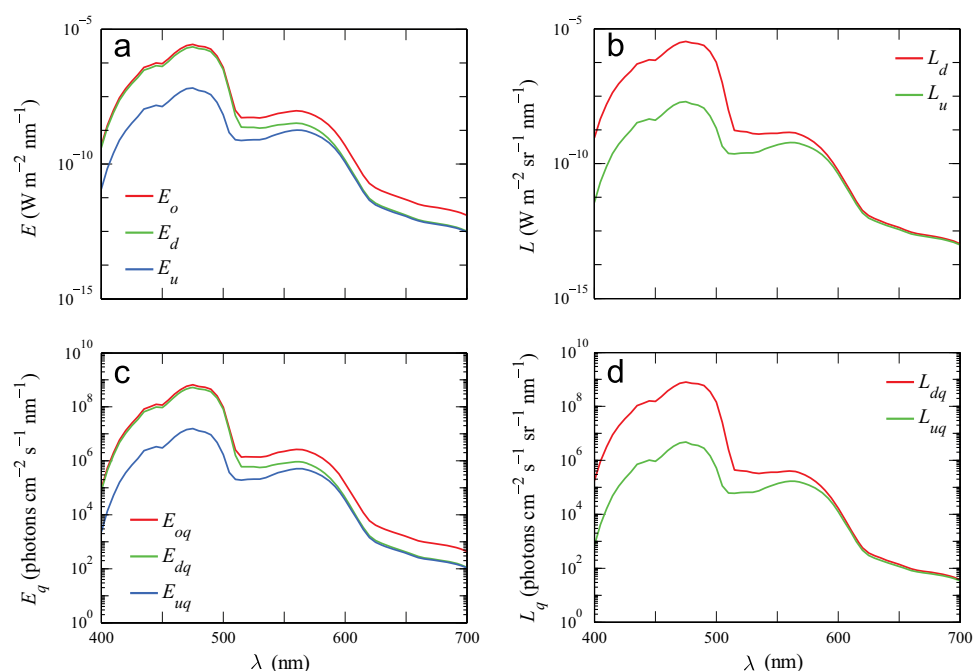


Fig. 12. (a) Spectra of the scalar irradiance $E_o(\lambda)$, downwelling plane irradiance $E_d(\lambda)$, and upwelling plane irradiance $E_u(\lambda)$, at 400 m depth from the simulation scenario of $\text{Chl}=0.2 \text{ mg m}^{-3}$ and clear sky conditions. (b) For the same simulation and depth, spectra of the downwelling vertical radiance $L_d(\lambda)$ and upwelling vertical radiance $L_u(\lambda)$. (c–d) Spectra of quantum irradiances and radiances corresponding to the data depicted in panels (a–b).

negligible effect on the mesopelagic light field in the blue spectral region (from 400 to about 500 nm), solar light at wavelengths exceeding 500 nm is dominated or originates entirely from Raman scattering and CDOM fluorescence. This has important implications for the patterns of the radiometric quantities and apparent optical properties observed within the mesopelagic zone.

Our simulations suggest that irradiance levels typically decline by about 9–10 orders of magnitude between the top and bottom of the mesopelagic layer. Most light propagating through this layer is contained within a relatively narrow spectral band of blue light with a maximum intensity at ~ 480 nm, and its angular distribution is dominated by downward traveling photons. This has implications for deep-sea animals, many of which possess upward looking eyes to utilize this portion of the light spectrum for vision. Light at longer wavelengths (i.e., $\lambda > 500$ nm) originates primarily from inelastic processes, have less directional aspect, and although generally significantly lower in magnitude than in the blue is still important for the overall characterization of the mesopelagic light field. One consequence of inelastic processes is that irradiance in the deep portion of the mesopelagic zone is higher at the long-wavelength end of the visible spectrum (red) than at the short-wavelength end of the spectrum (violet). In a hypothetical ocean without inelastic processes such a result would never be observed because the rapid absorption of red solar photons without replacement would dramatically lower the intensity of red light. In addition, Raman scattering within the mesopelagic zone produces a conspicuous secondary maximum in irradiance spectra with a peak around 565 nm. Another important consequence of inelastic processes is a nearly uniform angular distribution of mesopelagic light within the long-wavelength portion of the spectrum. This is also the case for the downwelling and upwelling light fields considered separately. However, unlike downwelling light, the upwelling light field is further characterized by an angular distribution that approaches a uniform distribution across the entire visible spectrum.

An important feature of the mesopelagic light field is that the angular distribution of spectral radiance and the apparent optical properties such as the spectral average cosines of the light field, diffuse attenuation coefficients for various radiometric quantities (i.e., radiance and different types of irradiance), and irradiance reflectance all become nearly constant with depth below a certain mesopelagic depth. This indicates that the light field approximates the asymptotic regime within the deeper portion of mesopelagic zone. The angular distribution of light and AOPs within this nearly-asymptotic regime exhibit weak or negligible dependence on the chlorophyll-*a* concentration and the IOPs in the surface ocean layer as well as boundary conditions at the sea surface. Our simulations suggest that it is reasonable to assume the existence of a nearly-asymptotic light field below depths of about 400–500 m. This assumption is further supported by additional contribution of an isotropic light background produced by radioactive decay of the unstable potassium isotope ^{40}K . Our results indicate that while the photons originating from solar radiation generally dominate over the light background produced by ^{40}K within the majority of mesopelagic zone, the latter is expected to dominate at greater depths below 1000 m. An important practical implication of the existence of the nearly-asymptotic regime is the ability to estimate the light field characteristics within the deeper portions of the mesopelagic layer (where the IOPs can be assumed to be typically nearly constant) from the extrapolation of vertical profile radiometric measurements which extend only to the top of the nearly-asymptotic field.

Acknowledgments

This study was supported by the U.S. Office of Naval Research (Grant N00014-09-1-1053) as part of the Department of Defense

Multidisciplinary University Research Initiative (MURI) Program. We thank C. Mobley and S. Johnsen for valuable discussions, F. Massa for providing numerical data on ^{40}K emission, and three reviewers whose comments led to improvements in the manuscript.

References

- Allen, J.J., Mathger, L.M., Buresch, K.C., Fetchko, T., Gardner, M., Hanlon, R.T., 2010. Night vision by cuttlefish enables changeable camouflage. *J. Exp. Biol.* 213, 3953–3960.
- Bartlett, J.S., Voss, K.J., Sathyendranath, S., Vodacek, A., 1998. Raman scattering by pure water and seawater. *Appl. Opt.* 37, 3324–3332.
- Berwald, J., Stramski, D., Mobley, C.D., Kiefer, D.A., 1998. Effect of Raman scattering on the average cosine and diffuse attenuation coefficient of irradiance in the ocean. *Limnol. Oceanogr.* 43, 564–576.
- Boden, B.P., Kampa, E.M., 1974. Bioluminescence. In: Jerlov, N.G., Steemann Nielsen, E. (Eds.), *Optical Aspects of Oceanography*. Academic Press, New York, pp. 445–469.
- Boden, B.P., Kampa, E.M., Snodgrass, J.M., 1960. Underwater daylight measurements in the Bay of Biscay. *J. Mar. Biol. Assoc. UK* 39, 227–238.
- Bray, A., Chapman, R., Plakhotnik, T., 2013. Accurate measurements of the Raman scattering coefficient and the depolarization ratio in liquid water. *Appl. Opt.* 52, 2503–2510.
- Bricaud, A., Morel, A., Babin, M., Allali, K., Claustre, H., 1998. Variations of light absorption by suspended particles with chlorophyll *a* concentration in oceanic (case 1) waters: analysis and implications for bio-optical models. *J. Geophys. Res.* 103, 31033–31044.
- Buskey, E.J., Swift, E., 1990. An encounter model to predict natural planktonic bioluminescence. *Limnol. Oceanogr.* 35, 1469–1485.
- Clarke, G.L., Denton, E.J., 1962. Light and animal life. In: Hill, M.N. (Ed.), *The Sea*. Interscience Publishers. John Wiley & Sons Ltd, New York, pp. 456–468.
- Clarke, G.L., Kelly, M.G., 1965. Measurements of diurnal changes in bioluminescence from the sea surface to 2000 m using a new photometric device. *Limnol. Oceanogr.* 10, R54–R66.
- Clarke, G.L., Wertheim, G.K., 1956. Measurements of illumination at great depths and at night in the Atlantic Ocean by means of a new bathyphotometer. *Deep Sea Res.* 3, 189–205.
- Cohen, J.H., Forward, R.B.J., 2009. Zooplankton diel vertical migration—a review of proximate control. In: Gibson, R.N., Atkinson, R.J.A., Gordon, J.D.M. (Eds.), *Oceanography and Marine Biology. An Annual Review*. CRC Press, Boca Raton, pp. 77–110.
- Denton, E.J., 1970. Review lecture: on the organization of reflecting surfaces in some marine animals. *Philos. Trans. R. Soc. Lond. Ser. B Biol. Sci.* 258, 285–313.
- Denton, E.J., 1990. Light and vision at depths greater than 200 m. In: Herring, P.J., Campbell, A.K., Witfield, M., Maddock, L. (Eds.), *Light and Life in the Sea*. Cambridge University Press, New York, pp. 127–148.
- Denton, E.J., Gilpin-Brown, J.B., Wright, P.G., 1972. The angular distribution of the light produced by some mesopelagic fish in relation to their camouflage. *Proc. R. Soc. Lond. Ser. B Biol. Sci.* 182, 145–158.
- Desiderio, R.A., 2000. Application of the Raman scattering coefficient of water to calculation in marine optics. *Appl. Opt.* 39, 1893–1894.
- Frank, T., Widder, E., 2002. Effects of a decrease in downwelling irradiance on the daytime vertical distribution patterns of zooplankton and micronekton. *Mar. Biol.* 140, 1181–1193.
- Frank, T.M., Case, J.F., 1988. Visual spectral sensitivities of bioluminescent deep-sea crustaceans. *Biol. Bull.* 175, 261–273.
- Frank, T.M., Johnsen, S., Cronin, T.W., 2012. Light and vision in the deep-sea benthos: II. Vision in deep-sea crustaceans. *J. Exp. Biol.* 215, 3344–3353.
- Frank, T.M., Widder, E.A., 1999. Comparative study of the spectral sensitivities of mesopelagic crustaceans. *J. Comp. Physiol. A* 185, 255–265.
- Gordon, H.R., Ding, K.Y., Gong, W.Y., 1993. Radiative transfer in the ocean: computations relating to the asymptotic and near-asymptotic daylight field. *Appl. Opt.* 32, 1606–1619.
- Gordon, H.R., Xu, X., 1996. Marine asymptotic daylight field: effects of inelastic processes. *Appl. Opt.* 35, 4194–4205.
- Gregg, W.W., Conkright, M.E., 2002. Decadal changes in global ocean chlorophyll. *Geophys. Res. Lett.* 29, <http://dx.doi.org/10.1029/2002GL014689>.
- Haddock, S.H.D., Case, J.F., 1999. Bioluminescence spectra of shallow and deep-sea gelatinous zooplankton: Ctenophores, medusae and siphonophores. *Mar. Biol.* 133, 571–582.
- Haddock, S.H.D., Moline, M.A., Case, J.F., 2010. Bioluminescence in the sea. *Annu. Rev. Mar. Sci.* 2, 443–493.
- Hawes, S.K., 1992. Quantum Fluorescence Efficiencies of Marine Fulvic and Humic acids (Master's thesis). University of South Florida, St. Petersburg, FL.
- Hawes, S.K., Carder, K.L., Harvey, G.R., 1992. Quantum fluorescence efficiencies of fulvic and humic acids: effects on ocean color and fluorometric detection. In: Gilbert, G.D. (Ed.), *Ocean Optics XI, Proceedings of the Society of Photo-Optical Instrumentation Engineers* 1750, Bellingham, WA, pp. 212–223, doi: 10.1117/12.140652.
- Hays, G.C., 2003. A review of the adaptive significance and ecosystem consequences of zooplankton diel vertical migrations. *Hydrobiologia* 503, 163–170.
- Herring, P.J., 1983. The spectral characteristics of luminous marine organisms. *Proc. R. Soc. Ser. B Biol. Sci.* 220, 183–217.

- Herring, P.J., 1996. Light, colour, and vision in the ocean. In: Summerhayes, C.P., Thorpe, S.A. (Eds.), *Oceanography*. Manson Publishing Ltd, London, pp. 212–227.
- Herring, P.J., Roe, H.S.J., 1988. The photoecology of pelagic oceanic decapods. *Symp. Zool. Soc. Lond.* 59, 263–290.
- Højerslev, N.K., Zaneveld, J.R.V., 1977. A Theoretical Proof of the Existence of the Submarine Asymptotic Daylight Field. Report 34. Copenhagen University Institute for Physical Oceanography, Copenhagen.
- Jerlov, N.G., 1976. *Marine Optics*. Elsevier Scientific Publishing Company, Amsterdam.
- Johnsen, S., 2005. The red and the black: bioluminescence and the color of animals in the deep sea. *Integr. Comp. Biol.* 45, 234–246.
- Johnsen, S., 2012. *The Optics of Life: A Biologist's Guide to Light in Nature*. Princeton University Press, Princeton.
- Johnsen, S., Sosik, H.M., 2004. Shedding light on light in the ocean. *Oceanus* 43, 1–5.
- Johnsen, S., Widder, E.A., Mobley, C.D., 2004. Propagation and perception of bioluminescence: factors affecting counterillumination as a cryptic strategy. *Biol. Bull.* 207, 1–16.
- Kampa, E.M., 1970. Underwater daylight and moonlight measurements in the eastern North Atlantic. *J. Mar. Biol. Assoc. UK* 50, 397–420.
- Kitchen, J.C., Zaneveld, J.R.V., 1990. On the noncorrelation of the vertical structure of light scattering and chlorophyll α in case I waters. *J. Geophys. Res.* 95, 20237–20246.
- Latz, M.I., Frank, T.M., Case, J.F., 1988. Spectral composition of bioluminescence of epipelagic organisms from the Sargasso Sea. *Mar. Biol.* 98, 441–446.
- Macdonald, A.G., 1975. Sensory physiology and buoyancy in the deep sea. In: Macdonald, A.G. (Ed.), *Physical Aspects of Deep Sea Biology*. Cambridge University Press, New York, pp. 199–264.
- Massa, F., 2002. Optical radiation background from ^{40}K decays in undersea neutrino telescopes. *Eur. Phys. J. C* 22, 749–756.
- McFall-Ngai, M.J., 1990. Crypsis in the pelagic environment. *Am. Zool.* 30, 175–188.
- Mobley, C.D., 1994. *Light and Water: Radiative Transfer in Natural Waters*. Academic Press, San Diego.
- Mobley, C.D., Sundman, L.K., 2008. *Hydrolight 5-Ecolight 5 Technical Documentation*. Sequoia Scientific, Inc, Bellevue.
- Mobley, C.D., Gentili, B., Gordon, H.R., Jin, Z., Kattawar, G.W., Morel, A., Reinersman, P., Stamnes, K., Stavn, R.H., 1993. Comparison of numerical models for computing underwater light fields. *Appl. Opt.* 32, 7484–7504.
- Morel, A., 1974. Optical properties of pure water and pure sea water. In: Jerlov, N.G., Steemann Nielsen, E. (Eds.), *Optical Aspects of Oceanography*. Academic Press, New York, pp. 1–24.
- Morel, A., Antoine, D., Gentili, B., 2002. Bidirectional reflectance of oceanic waters: accounting for Raman emission and varying particle scattering phase function. *Appl. Opt.* 41, 6289–6306.
- Myslinski, T.J., Frank, T.M., Widder, E.A., 2005. Correlation between photosensitivity and downwelling irradiance in mesopelagic crustaceans. *Mar. Biol.* 147, 619–629.
- Nelson, N.B., Siegel, D.A., Carlson, C.A., Swan, C.M., 2010. Tracing global biogeochemical cycles and meridional overturning circulation using chromophoric dissolved organic matter. *Geophys. Res. Lett.* 37, L03610, <http://dx.doi.org/10.1029/2009GL042325>.
- Ochakovskii, Y.E., Pelevin, V.N., Karlsen, G.G., Efimenko, I.D., Shitov, B.V., Shifrin, K.S., 1974. Rasprostranenie estestvennogo izlucheniya v okeane. In: Monin, A.S., Shifrin, K.S. (Eds.), *Gidrofizicheskie i Gidroopticheskie Issledovaniya v Atlanticheskom i Tikhom Okeanakh*. Izdatiye Nauka, Moskva, pp. 166–190.
- Petzold, T.J., 1972. Volume Scattering Functions for Selected Ocean Waters. SIO Reference 72–78. Scripps Institution of Oceanography, La Jolla.
- Pope, R.M., Fry, E.S., 1997. Absorption spectrum (380–700 nm) of pure water. II. Integrating cavity measurements. *Appl. Opt.* 36, 8710–8723.
- Preisendorfer, R.W., 1959. On the existence of characteristic diffuse light in natural waters. *J. Mar. Res.* 18, 1–9.
- Priede, I.G., Jamieson, A., Heger, A., Craig, J., Zuur, A.F., 2008. The potential influence of bioluminescence from marine animals on a deep-sea underwater neutrino telescope array in the Mediterranean Sea. *Deep-Sea Res. Part I: Oceanogr. Res. Pap.* 55, 1474–1483.
- Röttgers, R., Doerffer, R., 2007. Measurements of optical absorption by chromophoric dissolved organic matter using a point-source integrating-cavity absorption meter. *Limnol. Oceanogr.: Methods* 5, 126–135.
- Sogandares, F.M., Fry, E.S., 1997. Absorption spectrum (340–640 nm) of pure water. I. Photothermal measurements. *Appl. Opt.* 36, 8699–8709.
- Stramski, D., Reynolds, R.A., Babin, M., Kaczmarek, S., Lewis, M.R., Röttgers, R., Sciandra, A., Stramska, M., Twardowski, M.S., Franz, B.A., Claustre, H., 2008. Relationships between the surface concentration of particulate organic carbon and optical properties in the eastern South Pacific and eastern Atlantic Oceans. *Biogeosciences* 5, 171–201.
- Uitz, J., Claustre, H., Morel, A., Hooker, S.B., 2006. Vertical distribution of phytoplankton communities in open ocean: an assessment based on surface chlorophyll. *J. Geophys. Res.* 111, C08005, <http://dx.doi.org/10.1029/2005JC003207>.
- Vasilkov, A.P., Herman, J.R., Ahmad, Z., Kahru, M., Mitchell, B.G., 2005. Assessment of the ultraviolet radiation field in ocean waters from space-based measurements and full radiative-transfer calculations. *Appl. Opt.* 44, 2863–2869.
- Warrant, E.J., 2004. Vision in the dimmest habitats on Earth. *J. Comp. Physiol. A* 190, 765–789.
- Warrant, E.J., Locket, N.A., 2004. Vision in the deep sea. *Biol. Rev.* 79, 671–712.
- Werdell, P.J., Bailey, S.W., 2002. The SeaWiFS Bio-optical Archive and Storage System (SeaBASS): current architecture and implementation. In: Fargion, G.S., McClain, C.R. (Eds.), *NASA Technical Memorandum 2002-211617*. NASA Goddard Space Flight Center, Greenbelt, p. 45.
- Werdell, P.J., Bailey, S.W., Fargion, G.S., Pietras, C., Knobelspiesse, K., Feldman, G.C., McClain, C., 2003. Unique data repository facilitates ocean color satellite validation. *EOS Tran.* 84, 377–387, <http://dx.doi.org/10.1029/2003EO380001>.
- Widder, E.A., 2010. Bioluminescence in the ocean: origins of biological, chemical, and ecological diversity. *Science* 328, 704–708.
- Widder, E.A., Frank, T.M., 2001. The speed of an isolume: a shrimp's eye view. *Mar. Biol.* 138, 669–677.
- Zylinski, S., Johnsen, S., 2011. Mesopelagic cephalopods switch between transparency and pigmentation to optimize camouflage in the deep. *Curr. Biol.* 21, 1937–1941.